

Review

Open Access



Two-dimensional (2D) materials for 3D printed micro-supercapacitors and micro-batteries

Ghuzanfar Saeed^{1,#}, Taehun Kang^{1,#}, Jin Suk Byun^{1,#}, Donghyun Min¹, Jun Su Kim¹, Shrikant Vaiju Sadavar¹, Ho Seok Park^{1,2,3,*}

¹School of Chemical Engineering, Sungkyunkwan University, Suwon 440-746, Republic of Korea.

²SKKU Institute of Energy Science and Technology (SIEST), Sungkyunkwan University, Suwon 440-746, Republic of Korea.

³SKKU Advanced Institute of Nano Technology (SAINT), Sungkyunkwan University, Suwon 440-746, Republic of Korea.

#Authors contributed equally.

*Correspondence to: Prof. Ho Seok Park, School of Chemical Engineering, Sungkyunkwan University, 2066, Seoburo, Jangangu, Suwon 440-746, Republic of Korea. E-mail: phs0727@skku.edu

How to cite this article: Saeed G, Kang T, Byun JS, Min D, Kim JS, Sadavar SV, Park HS. Two-dimensional (2D) materials for 3D printed micro-supercapacitors and micro-batteries. *Energy Mater* 2024;4:400023. <https://dx.doi.org/10.20517/energymater.2023.81>

Received: 17 Oct 2023 **First Decision:** 5 Dec 2023 **Revised:** 30 Dec 2023 **Accepted:** 27 Feb 2024 **Published:** 18 Mar 2024

Academic Editor: Hao Liu **Copy Editor:** Yanbing Bai **Production Editor:** Yanbing Bai

Abstract

Two-dimensional (2D) materials display a unique set of physical/chemical properties and are considered potential building blocks for the manufacturing of microstructured materials for a number of applications. Prominent applications range from advanced electronics to miniaturized electrochemical energy storage devices (EESDs). Herein, we present a comprehensive and critical review of the recent developments in design and microfabrication of 2D-driven microscale electrodes for three-dimensional (3D)-printed micro-supercapacitors and micro-batteries. Firstly, we systematically discuss the advantages and disadvantages associated with various microfabrication techniques such as stereolithography, fused deposition modeling, inkjet printing, and direct ink writing. Next, key parameters disclosing the relationship between the characteristics of 2D-based materials and extrusion-driven 3D printing process for the development of versatile and sustainable EESDs are highlighted. 2D materials utilized for the construction of microelectrodes for supercapacitors (e.g., electric double layer capacitors (EDLCs), pseudocapacitors, and hybrid capacitors) and batteries (e.g., Li-based systems and next-generation systems, e.g., sodium-ion batteries and zinc-ion batteries) along with their prominent electrochemical contributions in relation to obtained 3D-printed architectures are discussed in detail. To promote the development of 2D materials-driven high-performance microscale EESDs, the relevant challenges and future research opportunities are also addressed.

Keywords: 2D materials, 3D printing, patterning, micro-supercapacitors, micro-batteries, energy storage



© The Author(s) 2024. **Open Access** This article is licensed under a Creative Commons Attribution 4.0 International License (<https://creativecommons.org/licenses/by/4.0/>), which permits unrestricted use, sharing, adaptation, distribution and reproduction in any medium or format, for any purpose, even commercially, as long as you give appropriate credit to the original author(s) and the source, provide a link to the Creative Commons license, and indicate if changes were made.



INTRODUCTION

The advent of wearable, integratable, and multifunctional microelectronics has urged the robust manufacturing of compatible microscale electrochemical energy storage devices (MEESDs) such as micro-supercapacitors (MSCs) and micro-batteries (MBs)^[1-4]. The key application areas of MEESDs are micro/nano-robots, microscale wireless sensors, implantable medical sensors, self-powered supply systems, smart cards, and patient positioning/tracking^[5-9]. It is very crucial to develop unique and sustainable micropower sources for newly emerging miniaturized electronics. The conventional electrochemical energy storage devices (EESDs) have sandwiched-like structure consisting of typical two electrodes, a separator, and an electrolyte, displaying certain inherited shortcomings of structures and size, which greatly hinders their applicability especially for the direct inclusion with microelectronics systems^[10-12]. To sort out this issue, it is imperative to introduce high-performance MSCs/MBs with compatibility and versatility with low-powered microelectronics systems. MEESDs, such as MSCs and MBs, are the optimum candidates that can be directly connected with microelectronics as independent microscale power systems^[13,14]. In addition, they can also be a supplement to miniaturized energy conversion (MEC) units such as nano-generators and solar cells^[15,16]. As a key component of the sustainable MEESDs, the electrochemical contributions of electrode materials play a crucial role in evaluating their overall performance. Thus, it is pertinent to design and fabricate novel high-rated MSC and MB electrode materials with excellent electrical conductivity characteristics and maximum charge storage capabilities. In this regard, two-dimensional (2D) materials are of significant importance in developing high-rated MEESDs owing to their high conductivity, large surface-to-volume ratio, recognized anisotropic properties, high specific surface areas (SSAs), and special characteristics to provide short diffusion pathways for electron/ion movement^[17-22]. In addition to their intrinsic features, 2D materials support the development of sustainable three-dimensional (3D)-printed microstructures due to their unique viscoelastic characteristics (\sim modulus of elasticity of 350-490 Pa), enhanced face-to-face stacking phenomena, with a large surface interaction that improves the intersheet interaction furthermore, and high aspect ratio (MXene \sim 4,000)^[23-27]. For scale-up fabrication of 2D materials-based MSCs and MBs, typical synthesis techniques such as doctor-blading and spin coating have restricted applications owing to their complicated synthesis process, high price, low efficiency, and high personnel requirements^[28,29]. Most importantly, with such manufacturing processes, it is quite a difficult task to meet the specific demands of customization and miniaturization. Therefore, introducing advanced manufacturing technologies for developing MSCs and MBs to meet the specific requirements of the modern microelectronics field is very pertinent. Based on the electrode architecture, MSCs/MBs are distinguished into two types: namely 2D (\sim or planar) and 3D (or nonplanar) devices^[30,31]. In comparison with 2D devices, 3D MEESDs can deliver maximum energy and power densities (PDs) because 3D architected electrodes enable the maximum loadings of electroactive materials and improve surface-to-volume ratios by minimizing electron/ion transportation distances^[32-34]. Xu *et al.* report the assemblance of graphene oxide (GO) 3D microstructure in an aqueous environment with minimum GO concentrations of 2 mg mL⁻¹ via hydrothermal reaction process^[35]. Hydrothermal reaction initiates the removal of some oxygen-based groups and weakens the existing repulsion forces between 2D functionalized graphene sheets (GSs), resulting in their cross-linked structure in the presence of van der Waals forces and hydrogen bonding. Moreover, GO sheets were also deployed to develop self-supported 3D microstructures based on other 2D nanomaterials [i.e., molybdenum disulfide (MoS₂), hexagonal boron nitride (*h*-BN), and C₃N₄]^[36]. In the past few decades, various other techniques were also employed to develop 3D-structured electrode materials, such as chemical vapor deposition (CVD), photo-patterning, wet/dry etching, physical vapor deposition (PVD), electrodeposition, atomic layer deposition (ALD), and sputtering^[37-43]. The main drawbacks associated with these techniques are the operational costs, limited materials selection, restricted template configurations (3D Ni foam), and poor design tailoring freedom for 3D-structured electrode materials. So, there is a need to emphasize simple, economical, and versatile advanced manufacturing techniques to develop high-performance 3D microstructured electrodes for sustainable MEESDs.

In comparison to traditional reported techniques, 3D printing technology, i.e., additive manufacturing (AM) process, which is an advanced bottom-up manufacturing technology possessing capability of developing geometrically intricate architectures with minimum operational costs and marginal wastage of materials as well^[44-46]. For 3D printing of microelectrodes, the printable inks based on electroactive materials are prepared, which can be printed as per defined electrode and cell designs including shapes, sizes, and architectures and finally are packaged with electrolyte filling. In detail, 3D-printed MEESDs could have the following unique characteristics; (A) they offer design freedom at the micron-sized dimensions, with the choice to develop any required shapes owing to the ability to develop complex architectures; (B) high areal and specific capacity values along with commendable ED/PD contributions owing to maximum areal loadings (up to 14 mg cm⁻²) of electroactive materials and maximized aspect ratio of the 3D-structured electrodes; (C) high ED/PD owing to the minimized ions/electrons diffusion channels facilitated by the 3D architectures of the printed electrodes; and (D) lower manufacturing cost compared to other manufacturing techniques, as 3D printing can drastically reduce wastage of materials with ultimate saving potential production time and also facilitate the direct integration of MSCs and MBs with microelectronics by eliminating assembly and packaging steps^[47-49].

With the subsequent development and adoption of new 3D printing techniques such as stereolithography (SLA), fused deposition modeling (FDM), direct ink writing (DIW), and inkjet printing (IJP), the assembly of 2D materials has been greatly diversified by providing more control for scalable fabrication of uniform microelectrodes and new directions for the development of 2D materials-based microstructures with required design/pattern and size^[50-53]. Thus, 3D printing techniques are expanding the application range of 2D materials-based MSCs and MBs by enhancing their performance and assisting the fast growth of sustainable MEESDs. This review report aims to cover in detail the key scientific/technical points and recent trends related to 2D materials to promote high-rated 3D-printed MEESDs, e.g., MSCs and MBs. It starts with an important introduction about the well-known 3D printing techniques (e.g., DIW, FDM, IJP, and SLA), mentioning their working mechanism, materials suitability, operation procedures, advantages, and deficiencies. In the subsequent section, we have summarized the crucial roles of 2D materials-based inks in the development of sustainable 3D-printed microelectrodes. In brief, these inks can improve controllability and tailorability of the resulting 3D-printed microelectrodes. By combining the versatile functions and valuable properties of 2D materials, it is possible to design and fabricate microstructures with unprecedented features covering the requirements of the advanced microelectronics industry. Finally, the impacts of various 2D materials (categorized based on energy storage mechanism), recent materials composition trends, and other prominent factors on the reported electrochemical contributions of 3D-printed MEESDs are well-outlined. These pre-mentioned various aspects make this review systematic and comprehensive by disclosing the role of 3D printing process and 2D materials-based structures in the development of high-rated MEESDs such as MSCs (electric double layer capacitors (EDLCs), pseudocapacitors, and hybrid capacitors) and MBs (Li/Na, and zinc-ion batteries) [Figure 1]. Subsequently, to expedite further research opportunities and development of sustainable and high-rated 2D materials-based MEESDs, the associated challenges are well-elaborated. Finally, various prospects are also suggested to further enhance the electrochemical performance of 3D-printed EESDs, e.g., by eliminating the use of binders, improving mechanical stability by controlling the generation of residual stresses in the printed layers, mitigating irreversible reactions, and unrevealing the in-depth intrinsic electrochemical energy storage mechanisms of the respective devices.

3D PRINTING TECHNIQUES

According to the International Committee of the American Society for Testing and Materials (ASTM), 3D printing processes are classified into seven prominent types established on their manufacturing principles:

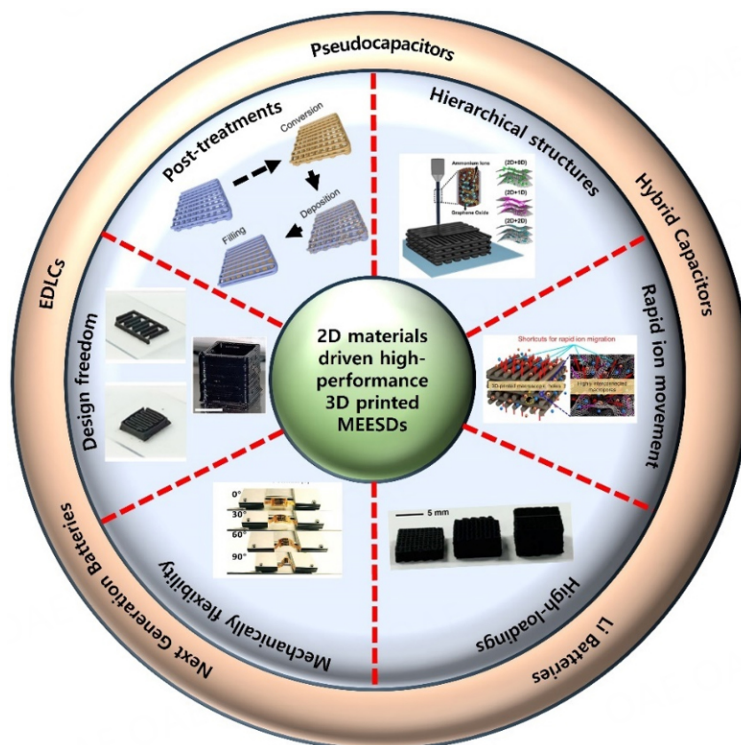


Figure 1. Schematic illustration of the organization of the review article outlining 2D materials for various 3D-printed MEESDs (e.g., micro-supercapacitors and micro-batteries).

(i) material jetting (e.g., aerosol jet printing and IJP); (ii) material extrusion (e.g., FDM and DIW); (iii) photopolymerization (e.g., two-photon lithography, SLA, and digital light processing); (iv) powder bed fusion (e.g., selective-laser-sintering); (v) sheet lamination (e.g., laminated object manufacturing); (vi) directed energy deposition (DED); and (vii) binder jetting (BJ)^[54,55]. Various high-standard reviews have been reported on various 3D printing technologies, outlining comprehensively their characteristics and properties. On the other hand, this review focused on exploring and epitomizing four 3D-printed technologies that have been deployed to manufacture MSC and MB modules to date, including FDM, DIW, IJP, and SLA. The printing technique can be picked up rationally pivoting on processability parameters and feature size of the key product to attain the customized architecture and outcome of the MEESDs (MSC and MB modules). So, in this regard, it is a key phenomenon to understand the printing processes and properties of different techniques for further technology and material design refinement. This review report summarizes the printing principles, benefits/drawbacks associated with prementioned printing techniques, in terms of applicable materials range, ink requirements, design versatility, throughput, resolution, multi-material capability, size capability, and cost.

Direct ink writing printing

Direct ink writing (DIW) printing is a pure example of extrusion-type deposition process, which starts with the preparation of viscoelastic ink with certain rheology characteristics and yield-stress behavior of the under-consideration raw material(s)^[56-59]. The printability of the deployed ink is crucial and mainly based on the sustainable mechanical behaviors of the MSCs and MBs and the rheological characteristics of the printed inks. In typical synthesis process of DIW, the customized 3D architectures are fabricated by extruding a filament of active material via a nozzle under variable pressure, and filament is stacked continuously on the particular substrate. The nozzle has the capacity to move horizontally in a two-axis

plane, and the platform can advance vertically downwards after the deposition of each new ink layer with the aid of computer-aided manufacturing (CAM) or computer-aided design (CAD) software. The diameter/size of the line in a printed pattern sketch depends on various printing parameters, e.g., air pressure, printing speed, nozzle diameter, and nozzle-substrate height. These pre-described parameters can be easily manipulated during the DIW printing process. Typically, DIW printing process parameters include applied air pressure of 5 psi, moving speed of 2 mm s^{-1} , $200 \text{ } (\mu\text{m})$ diameter of nozzle, and 0.15 mm nozzle distance from substrate. Moreover, printing resolution is normally decided by the provided extrusion pressure, nozzle diameter, and the properties of the printing ink. The potential of object molding is decided by considering the basic rheology characteristics of the ink, which involve the elastic/storage [G'] modulus, yield stress (δ_y), viscous/loss [G''] modulus, and viscosity ($\sim 10^6$ - 10^8 cP). Noteworthy, the yield stress response is the most crucial factor in curbing the volumetric flow rate and recovery characteristics of the printing ink after deposition and navigating the printing ability after yielding process. The inks display shear-thinning behavior, e.g., the viscosity reduces with increasing shear rates, and vice-versa characteristics of ink can be observed with decreasing shear rates. Viscosity is a basic rheological phenomenon to narrate the intermolecular interactions in the as-prepared ink. It is computed as a ratio of the shear stress to shear rate and thus can be smoothly exploited and quantified accordingly. In typical 3D printing process, inks possessing low viscosities can easily convert into droplet forms and will not display appropriate yield stress to strengthen the whole 3D-printed structure after the ink extrusion process, whereas the inks with high viscosities can comfortably clog the printing nozzle and need higher pressure for the development of microelectrodes. In conclusion, printing ink with appropriate high-viscosity and elastic behavior (assessed through G' and G'') is suitable for the 3D printing process, especially those that display shear-thinning characteristics. In comparison to other printing processes, DIW printing is most appropriate process to manufacture modules of MSCs and MBs owing to several outstanding printing advantages, which are summarized through following mentioned points [Figure 2A]^[60]: (i) DIW printing process provides wide design range with development of complicated 3D multi-scale frameworks; (ii) DIW process is flexible to print most of printing materials, ranging from metals to ceramics/plastics, hydrogels, and advanced functional materials (e.g., MXenes, graphene, metal-organic frameworks (MOFs), perovskite, and covalent organic frameworks), which provides numerous opportunities to print electroactive materials for MSCs and MBs; (iii) DIW printing has a potential to achieve a high-resolution (HR) printing process via microcapillary nozzles with a least diameter up to $1 \text{ } (\mu\text{m})$; (iv) DIW printing process facilitates multi-material printing-capability with high spatial and componential accuracy in the presence of diverse printing heads (e.g., switching, core-shell, and coaxial); and (v) DIW machines are available in varying grades with affordable purchasing costs with a simple controlled process. Thus, these pre-described characteristics hint that DIW process is the most appropriate choice for manufacturing versatile, high-performance, and sustainable MEESDs (MSCs and MBs). Despite these advantages, the most challenging factor regarding DIW printing process is the development of appropriate printing inks that display the combination of various technical characteristics outlining viscoelasticity, yield-stress behavior, and, most importantly, their unstoppable extruding process during applied pressure.

Fused deposition modeling printing

Fused deposition modeling (FDM) is another classical example of extrusion-driven printing processing through which layer-by-layer deposition of thermoplastic filaments can be attained. Thermoplastic filaments are heated to semi-molten conditions before they are extruded via nozzle on the substrate to develop 3D architectures^[61,62]. The different processing parameters utilized in the FDM printing process are layer height, wall thickness, infill pattern, infill density, printing speed, extrusion temperature, raster angle, raster width, and build orientation. FDM is the most frequent 3D printing process and is widely deployed in stationaries, toys, creative gifts, and training aids owing to its low costs and simple operation characteristics. In comparison to DIW printing process, FDM has a narrow window of printable materials and generally

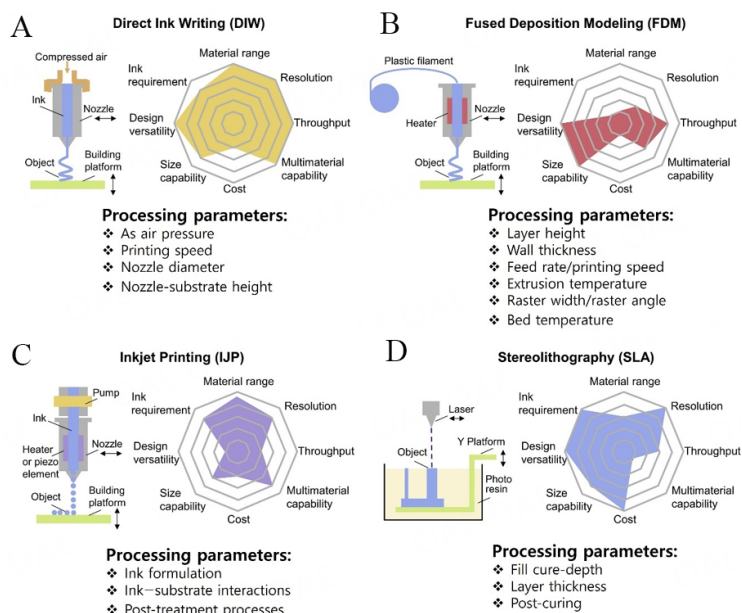


Figure 2. Schematic illustration of working principles and key characteristics of the prominent 3D printing processes for development of supercapacitors and batteries: (A-D) direct ink writing, fused deposition modeling, inkjet printing, and (D) stereolithography, respectively^[60].

needs thermoplastic filaments such as polyamide, acrylonitrile butadiene styrene, thermoplastic urethane, polycarbonate, and polylactic acid. These reported thermoplastic materials cannot be considered to develop sustainable electrodes for MSCs and MBs owing to their inferior electrical conductivity characteristics. Thus, to manufacture high-performance and sustainable MEESDs, it is required to consider and design useful filaments for FDM process. Various approaches have been reported to alter the basic characteristics of thermoplastic filaments in order to make them useful candidates for MEESDs; e.g., thermoplastic polymer matrices can be manipulated by mixing them with highly electroactive conductive materials. Besides this approach, electrochemical outcome of the extruded thermoplastic materials can also be enhanced by depositing advanced functional materials such as MXene and polypyrrole (PPy) or electrically conductive metals such as silver (Ag) and gold (Au)^[60]. Furthermore, in comparison to DIW printing techniques, the FDM also has low printing resolution (in the range of 50–200 μm), inferior flexibility of multi-material capability, and a lower printing throughput [Figure 2B]^[60].

Inkjet printing

Inkjet printing (IJP) is a typical class of deposition process where materials are directly propelled in the form of droplets via a nozzle onto plastic or paper-based substrates^[63]. This process is very much in similar to DIW printing, where printable ink is prepared first, which can be patronized by moving the printhead with nozzles across the provided platform with the assistance of the printer. The resolution of printed patterns is primarily ascertained by the rheological behavior of the utilized inks, along with the mechanism and physical operations related to the adopted fabricating process. In addition, the resolution of IJP printed patterns somehow also depends on the provided diameter of the printing nozzle, but a smaller diameter is costly to afford and more likely can cause clogging of the nozzle during printing process. Based on generated droplets, IJP currently has two main contemporary classes, namely continuous inkjet (CIJ) and drop-on-demand (DOD) IJP. By considering the working principle of CIJ, a continuous stream of printing droplets is generated under certain applied pressure and spread out on the provided platform. In comparison to DOD, the diameter of the droplet in CIJ is marginally bigger than that of printing nozzle,

resulting in an inferior resolution of the printed architectures. In contrast to CIJ, DOD has many advantages, e.g., HR, low operating costs, and atmosphere friendliness. In detail, the main reason of attaining HR of 20 μm is owing to pressure pulses created by piezoelectric or thermal printing heads. IJP inks also have some specific requirements in terms of dynamic viscosity and surface tension for printing process with reported much lower viscosities (typically in the range of 40 to 100 cP) than those deployed in DIW printing process. For productive control during the operation of printing process, a proper understanding of the ink behaviors outlining droplet formation, their spread processes, synergistic interactivity between the depositing droplet and the utilized substrate, and defect-free solidification process of droplets after deposition can impart significant roles^[64,65]. In comparison to FDM, abundant electroactive materials can be deposited through IJP printing process to develop MEESDs; however, the as-fabricated MEESDs are usually fabricated as thin films owing to low viscosities of utilized inks and size capability, which restricts the design and development of sustainable 3D-structured electrode materials [Figure 2C].

Stereolithography printing

Stereolithography (SLA) printing is a typical printing technique, which is purely based on photopolymerization process that produces the predefined 3D architectures by the application of a pre-designed scanning route of ultraviolet (UV) or visible laser source to the photoresin (typically acrylic or epoxy-based resin) followed by a solidification process^[66,67]. Usually, photosensitive precursor materials are based on two prominent components: a photoinitiator and a prepolymer material. In detail, UV light inaugurates the photopolymerization process of the respective resin, which then resulted in the formation of 2D single-layer cross-section after following the solidification process. The building platform unit moves vertically (upwards or downwards) to develop a monolithic component covered by a fresh layer of the liquid resin following the source of photo medium (UV or visible light), wherein the moving distance of the build platform is predefined by the height of the layer. The prominent processing parameters that can affect the quality of SLA-printed objects are fill cure-depth, layer thickness, and post-curing. Through SLA printing process, 3D objects are completed with the assistance of each newly cured layer according to the pre-designed model of the architecture. After the process, these objects are washed properly with appropriate solvent to remove the wet uncured resin from their respective surfaces before the post-processing is initiated. However, for the smooth completion of the process, photopolymerization process should involve a perfect photoinitiation process and support a fast-crosslinking process, so that on exposure to light, solidification of liquid resin should immediately occur to form highly cross-linked networks^[68]. Therefore, the right ratio of photoinitiators and prepolymer materials in the liquid resin is very crucial. Considering the working mechanism of SLA printing process, the printable resins are aggregates of photoinitiators, prepolymers materials, and electroactive materials. Moreover, in comparison to other printing techniques such as DIW, IJP, and FDM, the SLA technique has lower resolution and can print objects with a minimum feature size of approximately 0.5 mm. The prominent areas of application of SLA in the development of MEESDs include: (i) the preparation of collectors and substrates to fill electrode materials or deposit conductive layers; and (ii) blending of light-treatable polymeric materials with electroactive materials. In contrast to IJP and DIW printing processes, SLA does not rely on nozzles to develop printed objects; thus, it does not have any conventional clogging problems [Figure 2D]. SLA printing process has various advantages such as being easy to operate and having improved resolution; however, its commercial application is highly restricted and minimal owing to the handling of sticky and messy processes involved in preparing photopolymers.

2D MATERIALS FOR SUSTAINABLE 3D-PRINTED MICROSTRUCTURES

Distinct characteristics

Owing to unique printing aspects of DIW process, the importance of 2D materials will be disclosed in relation to the preparation of sustainable and high-performance 3D-printed architectures. For DIW, various

steps starting with ink preparation, ink extrusion, deposition/solidification of extruded filament, post-processing cycles play a crucial role in the successful printing process of materials or devices. In contrast to other 3D printing processes, solidification of DIW-printed filament purely depends on self-supporting behaviors of printing inks. So, appropriate properties of printing inks become the most considerable requirement for continuous extrusion and sustainability of self-supported 3D-printed filaments^[69]. In the meantime, to attain commendable electrochemical performance and high quality of DIW-printed MSCs and MBs, some important technical/scientific phenomena need to be addressed as disclosed followingly. Initially, ink composition should be rationally designed and formulated. In this regard, electroactive materials, additives (e.g., cross-linkers, binders, and fillers) and solvent mediums are the prominent components that are either physically or chemically mixed together to formulate the printing inks. Among various dimensional [zero-dimensional (0D), one-dimensional (1D), 2D, and 3D] available electroactive materials, 2D materials-based inks possess unique physicochemical characteristics. Their high electrical conductivity can accelerate electron transportation; enhanced specific surface areas can facilitate the adsorption of ions resulting in maximum capacitance, and tunable interlayer spacing supports ion intercalation. In addition to these pre-described physicochemical properties, these also have a large surface-to-volume ratio, recognized anisotropic properties, high mechanical strength and chemical stability, enhanced face-to-face stacking phenomena (with a large surface interaction that improves the intersheet interaction furthermore), shorter ion transportation pathways (supported by their exposed contact between microscale electrodes and electrolytes), and high aspect ratio (MXene $\sim 4,000$)^[70-72]. All these pre-mentioned characteristics are quite important for the development of sustainable MEESDs.

Unique rheological properties and printing design freedom

In addition to the distinct merits of 2D-structured materials, appropriate ink rheological characteristics are fundamental requirements for the continuous ink fluidity and retainment of filament printed shape since inks have to undergo three prominent steps during DIW printing process, including flow of inks inside the syringe and nozzle, extrusion of the provided inks through the nozzle and subsequently deposition on the provided substrate. During the DIW printing process, a smooth flow of ink inside the syringe and nozzle must be ensured to avoid any kind of clogging during ink extrusion process. In general, the viscosities of printing inks decreased with increasing shear rates, which favors both processes namely ink flow from nozzle and ink extrusion. Furthermore, 2D materials-driven inks are proven to display shear-thinning characteristics by rationally designing the formulation of their respective solutions. In addition, it has also been reported that 2D materials contribute unique rheological properties mainly supported by their high aspect ratio. For instance, GO displayed an excellent modulus of elasticity of 350-490 Pa in water with a reported concentration of 13.3 mg mL⁻¹ in comparison to the lower elastic modulus (~ 60 Pa) of 1D material-(single-walled carbon nanotube) SWCNT suspension with the same concentration^[73]. Owing to several advantages associated with 2D-driven inks such as their unique rheological characteristics and ease of manipulating colloidal response, it is well concluded that 2D materials are the most appropriate contenders for manufacturing 3D architectures with required design and optimized electrochemical properties^[74].

To date, development of 2D materials-driven microstructures via 3D printing process is mainly based on graphene-based microelectrodes, and GO-driven ink is commonly utilized. Generally, the viscoelastic characteristics of GO in water are mainly dependent on its concentration and have been extensively investigated to obtain different ink printabilities contributions according to the adapted process and purpose [Figure 3A-D]. In this context, Tian have concluded that with low concentrations (0.05 to 0.25 mg mL⁻¹), GO possessed a slightly lower elastic modulus (G') than its viscous modulus (G''), displaying a typical liquid-like response, which is more suitable for conventional technique such as spray coating but cannot favored 3D printing process where printed microstructures need to retain itself

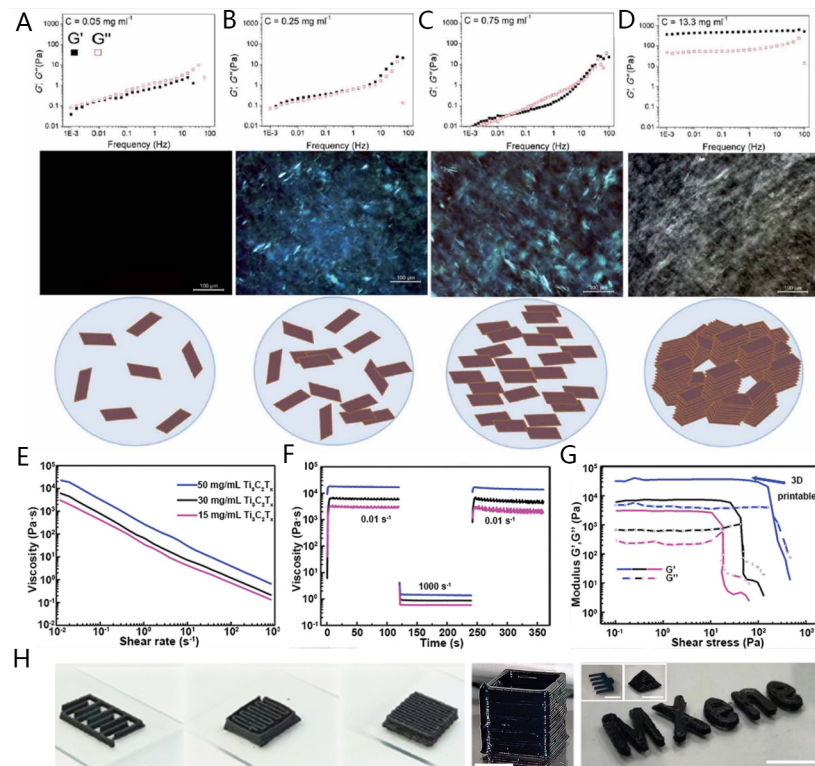


Figure 3. (A-D) storage moduli (G') and loss moduli (G'') of graphene oxide (GO) suspensions of frequency at different concentration degrees; e.g., 0.05, 0.25, 0.75, and 13.3 mg mL⁻¹, respectively^[75]; (E) MXene-based inks (with various concentrations) shear thinning behaviors suitable for uninterrupted extrusion through printing nozzles (diameter ~250 μ m); (F) inks viscosity evolution over time for alternate minimum (0.01 s⁻¹) and maximum (1,000 s⁻¹) shear rates, illustrating suitable viscosity drop and post-printing recovery; (G) inks' viscoelastic fingerprints demonstrating their solid-like behavior with large plateau regions (where G' is unhampered of stress) and yield stresses (overlap point between G' and G'') that elevate as the inks become more thickened (concentrated)^[79]; and (H) illustration of 2D materials-based 3D-printed architectures: serpentine electrode, woodpile electrode (scale-bar = 10 millimeter), rectangular-like hollow prism printed through 250 μ m nozzle (number of printed layers = 25, reported scale-bar = 3 millimeter), and pectinate structure (two printed layers, scale-bar = 10 millimeter)/pyramid-like 3D-printed structure (number of printed layers = 12, scale-bar = 10 millimeter)/MXene printed font (three printed layers, scale-bar = 10 millimeter)^[79,83,84].

[Figure 3A and B]^[75]. Further slight increase in concentration up to 0.75 mg mL⁻¹, the fluid characteristics of GO are appropriate for IJP process [Figure 3C], while weak gel-like materials are attainable up to 2.5 mg mL⁻¹. However, due to considerable increase in concentration up to 13.3 mg mL⁻¹, G' is improved significantly in comparison to G'' , and GO ink starts to act akin to a viscoelastic liquid crystal (LC) gel with commendable elastic modulus and viscosity. Under this ideal situation, GO ink has the capability to pass through the nozzle under a high strain rate and solidifies immediately to support its structure once it is printed through DIW process [Figure 3D]. Thus, this study clearly illustrates the importance to control the rheological characteristics to obtain sustainable microstructures for EESDs. Additives such as secondary surfactants or solvents are always added into inks based on graphene, carbon nanotubes (CNTs), and MoS₂ to regulate their rheological characteristics for 3D printing process. However, their addition can significantly affect the electrochemical characteristics of the as-developed printed microelectrodes. In these circumstances, a new group of 2D materials such as MXenes can significantly impart their role to develop additive-free 3D-printed microelectrodes owing to their following described outstanding physical and chemical contributions. MXenes exhibit excellent electrical conductivity, robust mechanical strength, phenomenal redox activity, and rich surface functional groups. The surface functional groups not only promote their hydrophilic behavior but also provide active sites for rapid redox reactions. Furthermore, in

comparison to other 2D materials, MXenes have a high aspect ratio ($\sim 4,000$), which is beneficial to attain their high viscosity behavior even at moderate concentrations^[76-78]. The rheological behavior of MXene-driven inks has been well-probed to determine their suitability for the 3D printing process [Figure 3E-G]^[79]. Similarly, to GO-based inks, the viscosity and viscoelastic characteristics of MXene-driven inks also depend on their concentration of $Ti_3C_2T_x$ flakes in water. Moreover, inks clearly demonstrate shear-thinning behavior [Figure 3E] coinciding with typical reported 2D materials. The viscosity recovery of shear-thinning MXene-based inks over time further validates their capability for uninterrupted extrusion process occurring during 3D printing cycle [Figure 3F]. By asserting alternatively 0.01 s^{-1} (low) and $1,000\text{ s}^{-1}$ (high) shear-rates to the inks over provided time, the viscosity of the inks drops at higher shear rates (featuring extrusion via narrow nozzles), and instantaneous recovery in the inks occurs in the presence of reduced shear rates (featuring post-printing recovery of rheological characteristics of inks). The predominately solid-like behavior of MXene-based ink is confirmed through its viscoelastic fingerprints with maximum storage modulus (G') at the plateau region of Figure 3G (herein, G' does not depend on stress confirming the development of a highly permeate network of $Ti_3C_2T_x$). The attained viscoelastic network of MXene disrupts and starts flowing under a critical applied stress level (the yield stress at a certain crossover point between G' and G''), generating liquid-like characteristics ($G'' > G'$) of ink, enabling its continuous extrusion via meter-micron-sized nozzles during printing process. In conclusion, the magnitude of the elastic modulus and yield stress of the as-prepared inks improve with higher ink concentration through 2D MXene flakes, supporting the sustainability of printed structures formed through continuous extrusion process. For MXene-driven inks with concentrations up to 50 mg mL^{-1} , elastic modulus and yield stress stretch out to 36,507 and 206 Pa, respectively, comparable to other reported inks for other 2D-based systems^[80-82]. Highly functional 2D inks with increased material loadings possess appropriate viscoelastic behavior and can easily glide via provided narrow nozzles, instantaneously displaying their solid-like characteristics to retain filamentary geometry of the nozzle after the completion of extrusion process. As a consequence, it is possible to deposit layer-by-layer configuration of 2D inks to construct 3D diverse and complicated printing architectures such as a serpentine electrode, woodpile structure, rectangular hollow prism, and pectinate structure/pyramid/MXene font [Figure 3H]^[79,83,84].

Hybridization and post-processing treatments

The hybridization of advanced materials can facilitate synergistic effects to accelerate performance far beyond those consisting of individual components for the development of sustainable electrochemical energy storage. In this regard, 2D materials, such as graphene, own great potential as a building block for the development of 3D macroscopic architectures by the inclusion of various dimensional secondary materials (for instance, 0D, 1D, and 2D functional additives). However, to fully investigate the potential of these hybridized 3D structures, various parameters should be prioritized in the design process: (i) agglomeration of functional groups should be controlled on the surface of a building block in order to facilitate massive electroactive sites; (ii) the configuration can be molded easily in curved geometries or 3D complex architectures; and (iii) well-interconnected networks are desirable in comparison to the disintegrated and crumbled architectures to improve performance parameters such as mass deposition and rapid charge transportation. Conventional synthesis techniques, such as self-assembly (e.g., polymer promoters-assisted cross-linking, hydrothermal, and chemical reduction) and templated-assisted approach (emulsion, nickel foam, and ionothermal template), have not proven worthy enough to attain the pre-mentioned requirements for high-performance macroscopic 3D architectures. DIW is an advanced and versatile manufacturing process and provides greater opportunities in the development of 3D mixed-dimensional hybrids at the macroscopic scale. Tang *et al.* reported the successful synthesis of DIW-printed graphene-driven mixed-dimensional (2D + 0D \sim graphene/Ag, 2D + 1D \sim graphene/multi-walled CNTs (MWCNTs), and 2D + 2D \sim graphene/MoS₂) hybrid aerogels (G-MDHA) for high-performance MSCs [Figure 4A]^[85]. The field-emission scanning electron microscope (FE-SEM)/transmission electron

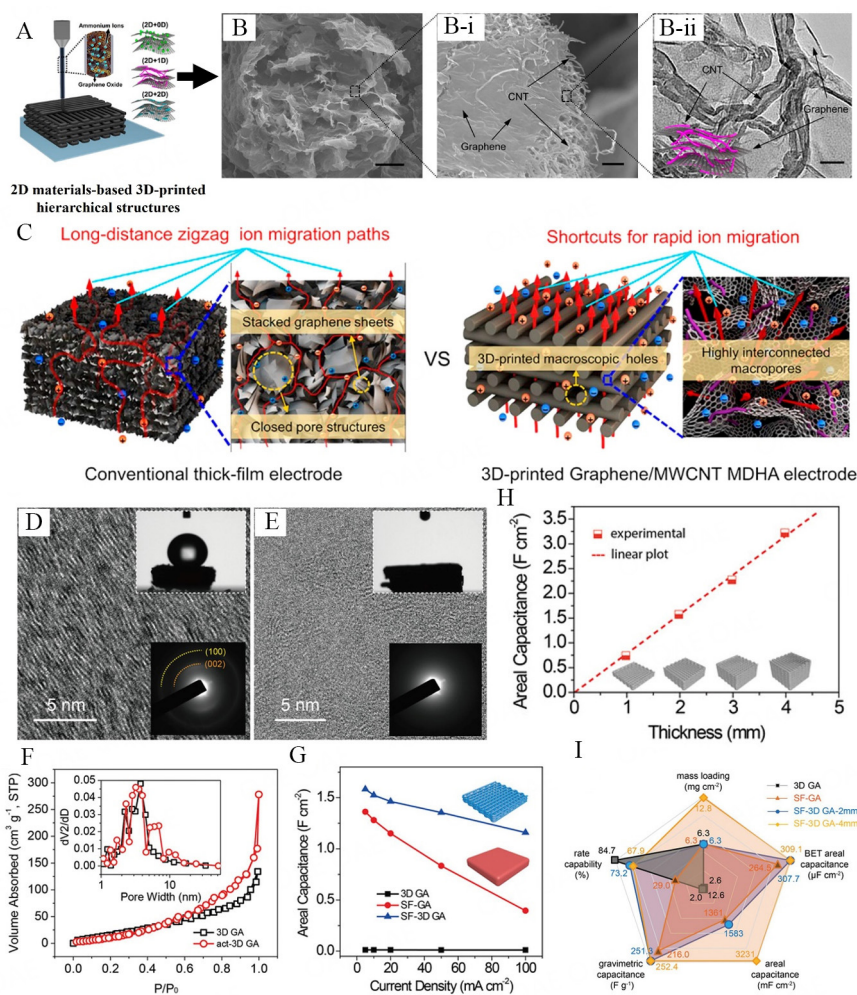


Figure 4. (A) Schematic illustration of 2D materials-based 3D-printed hierarchical structures; (B-i) FE-SEM images of (2D + 1D) graphene-CNTs mixed hybrid material at various magnifications (scale bar: 50 μm and 200 nm, respectively); (B-ii) TEM microstructure of graphene-CNTs mixed hybrid material with inset of schematic illustration of 2D + 1D hybrid material (scale bar: 40 nm); (C) Schematic demonstration of insufficient and sufficient ion migrations for conventional thick-film and DIW advanced graphene-MWCNTs hybrid electrode materials, respectively^[85]; (D and E) TEM microstructures of the 3D GA and SF-3D GA samples, respectively; (F) Nitrogen adsorption-desorption isotherms of the 3D GA and SF-3D GA samples, while inset displays pore-size distribution plots of the respective samples; (G) Areal capacitance contributions of 3D GA, SF-GA, and SF-3D GA reported at various current densities; (H) Areal capacitance of SF-3D GA electrode materials as a consequence of electrode varied thickness reported at 5 mA cm^{-2} ; and (I) a radar chart illustrates the five points of performance comparison including mass loadings of the electrode materials, BET surface area, specific capacitance (F g^{-1}), areal capacitance (mF cm^{-2}), and rate-capability (~5 to 100 mA cm^{-2}) of 3D GA, SF-GA, and SF-3D GA^[86].

microscope (TEM) microstructure analysis of graphene/MWCNTs hybrid electrode material is displayed in [Figure 4B(B-i and B-ii)]. The DIW-printed MDHA filament has well retained its cylindrical geometry [Figure 4B]. Moreover, GSs are well separated owing to the existence of MWCNTs, facilitating a number of micropores within the structure of MDHA. Owing to the existence of strong π - π interaction between 1D MWCNTs and 2D GSs, the electrical conductivity of graphene/MWCNT MDHA was enhanced from 40 to 120 S m^{-1} with a density of 60 mg cm^{-3} . The as-prepared graphene/MWCNT MDHA was utilized to assemble a coin cell-like symmetric supercapacitor. The symmetric supercapacitor device had shown a commendable areal capacitance value of 639.56 mF cm^{-2} at 4 mA cm^{-2} , with phenomenal rate-capability of 71.4% at 40 mA cm^{-2} . The reasons for the improved rate-capability performance contributions of graphene/MWCNT MDHA are well schematically illustrated in [Figure 4C]. In conventional thick-film electrode

materials, irregular and snaky networks have resulted in the formation of blind and closed porous structure, which do not allow the consistent access of electrolyte solution, resulting in the wastage of the utilized electroactive material. However, on the other side, 3D-printed architecture consisting of well-interconnected hierarchical porous networks allows unobstructed pathways for ion transportation from the foundation to the uppermost surface of the graphene/MWCNT MDHA. Moreover, properly interfaced adjacent filaments of 3D-printed architecture and strong interaction between MWCNTs and GSs also support well-defined pathways for electron transportation. In the context of hybridization of 2D materials to manufacture high-performance MEESDs, Yu *et al.* reported the development of 3D-printed architecture based on NiCoP/MXene (NCPM) for EESDs with maximum volumetric and areal energy density (ED) outcomes^[2]. The impact of hybridization is clearly illustrated through the reported electrochemical performance of nickel cobalt (NC)-layered double hydroxide (LDH) nanowires, NC phosphate (NCP) nanowires, and NCPM with their reported specific capacitances of 608, 920, and 1,359 F g⁻¹, respectively, at 1 A g⁻¹. The obtained superior electrochemical performance of NCPM is owing to the rational incorporation of MXene scaffolds, which improves the electrical conductivity and provides appropriate open channels for rapid movement of electrons/ions in hybrid architecture. These pre-mentioned characteristics also helped NCPM to attain its maximum rate-capability of up to 79.6% at 10 A g⁻¹.

The significance of post-processing steps in order to enhance the electrochemical contribution of DIW-printed architectures cannot be ignored. For 3D extruded microstructures, widely reported post-treatment processes such as thermal annealing, surface-functionalization, and surface polishing (or deposition) are deployed. As mentioned earlier, most of the graphene-driven DIW-printed microelectrodes are based on GO dispersions, hinting at the low electrical conductivity and inferior rate-capability of directly extruded GO filaments. In this context, Yao *et al.* deployed a unique combination of thermal annealing and surface functionalization in order to enhance the overall electrochemical contributions of 3D graphene aerogels (SF-3D GA)^[86]. In detail, 3D-printed microstructures were properly freeze-dried and annealed at a temperature of 1,050 °C to transform GO aerogels into graphene-driven aerogels. In the next development step of SF-3D GA, the graphene aerogels were electrochemically oxidized in the presence of 0.5 M KNO₃ solution in order to introduce surface functional groups for particular time of 3 h. Finally, surface functionalized 3D GA was further reduced in hydrazine hydrate (HH) solution (0.1%) for 1 h at 50 °C. The impact of electrochemical oxidation has not significantly changed the structure and nanosheets' morphology of the 3D-printed architecture. However, HR-TEM microstructure clearly illustrates that crystallinity level of GSs reduces after the electrochemical oxidation process [Figure 4D and E]. Comparing SAED patterns (bottom inset of Figure 4D and E) also confirms the amorphous nature of the graphene nanosheets of the SF-3D GA sample. Moreover, contact angle measurements (top inset of Figure 4D and E) illustrate that 3D GA has changed from hydrophobic nature (~contact angle 140°) to hydrophilic (~contact angle 0°) after the commencement of electrochemical oxidation process. As per nitrogen adsorption-desorption isotherms, the SSA value of 3D GA architecture has also improved moderately from 78.3 to 81.7 m² g⁻¹ after the commencement of surface modifications of graphene nanosheets [Figure 4F]. The SF-3D GA sample has a significant amount of mesoporous with a width ranging between 4 to 8 nm (inset of Figure 4F), which is well in accordance with its reported TEM result. The electrochemical performance comparison among 3D GA, SF-GA, and SF-3D GA samples is illustrated in Figure 4G. The SF-3D GA delivered a high areal capacitance (C_a) value of 1,583.2 mF cm⁻² at 5 mA cm⁻², which is almost 125-fold tall than the reported areal capacitance (12.6 mF cm⁻²) value of 3D GA sample at the same current density (CD) value. The SF-3D GA sample also retained an areal capacitance of 1,159.2 mF cm⁻² [with a reported volumetric capacitance (C_v) of 5.8 F cm⁻³] at 100 mA cm⁻². Furthermore, the edge of SF-3D-printed GA is also confirmed through the attained linear relationship between the electrochemical performance (areal capacitance) and thickness of the electrode material [Figure 4H]. The SF-3D GA sample with a maximum thickness of 4 mm and areal mass loading of 12.8 mg cm⁻² contributed an excellent areal capacitance value

of $3,231 \text{ mF cm}^{-2}$ at 5 mA cm^{-2} . The reported areal capacitance performance is much improved in comparison to other carbon-driven electrode materials such as activated carbon (AC) fibers ($\sim 1,385 \text{ mF cm}^{-2}$)^[87], 3D-printed hierarchical microporous graphene aerogels ($\sim 206.7 \text{ mF cm}^{-2}$)^[88], 3D-printed carbon aerogels structures (645 mF cm^{-2})^[89], and highly AC cloth (88 mF cm^{-2})^[90]. The remarkable electrochemical performance of SF-3D GA with maximum mass loadings is owing to its activated and porous structure that allows maximum accessibility of ions per unit mass in its 3D-printed architecture. Finally, [Figure 41](#) illustrates the radar chart that compares various points of merits such as mass loading, areal capacitance (C_a) normalized to the geometric surface area, gravimetric capacitance, areal capacitance normalized to brunauer–emmett–teller (BET) surface area, and rate-capability of various 3D-printed graphene-aerogels. Owing to the enriched pseudocapacitance contributions mainly from functional groups, the SF-3D GA-2 mm has simply achieved high gravimetric and areal capacitance in comparison to the 3D GA-2 mm sample. In addition, the SF-3D GA sample areal capacitance value is doubled with the rise of its thickness from 2 to 4 mm (with a doubled amount of active material). In conclusion, the SF-3D GA sample has contributed to high-rate capability, endorsing the importance of 3D-printed architectures for enhancing the capacitance contributions of electrode materials with high mass loadings at higher CD values. Moreover, another study conducted by Yao *et al.* has also illustrated the importance of post-treatments in order to enhance the electrochemical contributions of 2D materials-driven 3D-printed microstructures^[57]. Initially, GO-based microstructures were fabricated by DIW printing process. Subsequently, printed architectures were freeze-dried to develop aerogels, followed by an annealing process in the existence of nitrogen to transform GO to graphene ($\sim 3\text{D G}$). In the final step of applied post-treatment process, MnO_2 nanosheets were successfully electrodeposited onto the printed graphene aerogel (denoted as 3D G/ MnO_2 hybrid material). The reported electrochemical performance (in terms of areal capacitance, $\sim C_a$) of 3D G/ MnO_2 was almost 25 times higher in comparison to 3D G evaluated in 3 M LiCl electrolyte solution. Such phenomenal electrochemical output of 3D G/ MnO_2 hybrid material is associated with its 3D porous architecture, which is extremely conductive and suitable for the electrolyte and ions diffusion in the existence of pseudocapacitive MnO_2 nanosheets. Besides this, the deposition of ultrathin MnO_2 nanosheets has also increased the SSA of the G-printed aerogel architecture up to $100 \text{ m}^2 \text{ g}^{-1}$. More importantly, the areal capacitance (C_a) of the 3D-printed G/ MnO_2 hybrid material improves linearly with the mass loadings of MnO_2 ($\sim 182.2 \text{ mg cm}^{-2}$) and electrode thickness (4 mm), illustrating that the capacitive outcome is not restricted by ion diffusion.

2D MATERIALS FOR 3D-PRINTED MICRO-SUPERCAPACITORS

2D materials for 3D-printed EDLCs

Utilizing 2D materials as electrodes in EDLC-based MSCs offers a plethora of advantages that collectively contribute to the remarkable enhancement of device performance and capabilities^[91]. Commonly, in EDLCs-driven MSCs, energy is physically stored via electrostatic charge adsorption at the two-phase interface existing between the electrolyte and electrode material. MSCs based on EDLC materials exhibit a lofty SSA value of $2,630 \text{ m}^2 \text{ g}^{-1}$, excellent PD, phenomenal electronic conductivity, and unmatched cycle life^[92]. Furthermore, these MSCs offer rapid charging and discharging rates, enabling efficient energy transfer within remarkably short timeframes^[93]. The low internal resistance of EDLCs allows them to promptly respond to sudden energy requirements, positioning them as invaluable assets in applications requiring instantaneous surges of power, such as peak power compensation and the management of pulsed loads in electronic systems^[94]. Considering the content of the article, herein, we have emphasized the importance of 2D-driven EDLC materials (e.g., graphene, graphene-driven composites, and GO) for the development of sustainable 3D-printed MSCs. In detail, various approaches have been disclosed in forthcoming sections deployed to fabricate high-performance and sustainable graphene-driven 3D-printed architectures. In this regard, Jiang *et al.* have fabricated graphene aerogel microlattices (GAMs), which show immense promise across multifunctional applications owing to their combination of low density, high

porosity, precisely engineered lattice structures, exceptional elasticity, and adjustable electrical conductivity^[95]. However, previous 3D printing methods for creating GAMs have been hindered by either the need for a high concentration of additives or intricate fabrication processes, limiting their widespread utility. This study introduces a straightforward ion-induced gelation technique for directly 3D printing GAMs using GO-based ink. By introducing a small quantity of Ca^{2+} ions as gelators, the aqueous GO solution undergoes a transformation into a printable gel ink. This ink is utilized to directly print self-supporting 3D structures, featuring programmable microlattices, within ambient air conditions at room temperature. The as-developed microlattices were freeze-dried to develop solid GO aerogel, which was further reduced in the existence of hydrogen iodide (HI) to obtain cleaned 3D-printed graphene-driven microlattices [Figure 5A]. In order to study the mechanical behavior, compression tests were performed to gauge the compressive stress as a result of reported strain of the 3D-printed GO aerogel samples. Compression results show that the 3D-printed GO aerogels display phenomenal resilience when liberated from compression cycle. At 80% strain, 3D-printed GO architecture has displayed a compressive stress value of ~ 90 kPa [Figure 5B]. The resultant GAMs possess a complex hierarchical pore structure alongside high electrical conductivity, translating into impressive capacitive performance well-suited for supercapacitors. The cyclic voltammetry (CV) curves of the 3D graphene-driven supercapacitor (3DGC) electrodes produced using the formulated ink display near-square shapes, a clear indication of the expected performance associated with EDLC [Figure 5C]. The gravimetric capacitance of 3DGCs is reported to be 212 F g^{-1} at 1 A g^{-1} . Moreover, the impact of electrode thicknesses (300, 900, and $1,500 \mu\text{m}$ as 3DGCs-1, 3DGCs-2, and 3DGCs-3, respectively) was also well-investigated on the rate-capability contributions of 3DGCs [Figure 5D]. Interestingly, all 3DGCs displayed capacitance retention over 80% at 100 A g^{-1} ; however, 3DGCs-1 contributed highest rate-capability up to 86% among all reported samples. A possible reason for the degradation of rate-capability contributions of 3DGCs is the increase of equivalent series resistance with the increase of electrode thickness. Notably, the capacitive performance remains stable, with over 90% capacitance retention after an extensive 50,000 charge-discharge cycles. The ability to 3D printing needs neat GO; using a facile and direct approach holds the potential to expand the applications of GAMs across domains ranging from energy storage to the creation of scaffolds for tissue engineering. Remarkably, these GAM structures exhibit an impressive 90% capacity retention over 50,000 cycles, confirming their exceptional cycling stability.

Another study conducted by Tang *et al.* has reported 3D-printed graphene aerogel and graphene-driven mixed-dimensional hybrid aerogels for supercapacitors^[85]. Herein, the main disclosed concept is to illustrate the importance of graphene-driven mixed-dimensional (2D + 0D, 2D + 1D, and 2D + 2D) electrode materials for the evolution of high-performance 3D-printed electrode materials. The adopted procedures to control the rheological characteristic of the printing inks (GA and G-MDHA) and development of 3D-printed GA and G-MDHA architectures are well illustrated in Figure 5E. Further synthesis protocols of 3D GA and G-MDHA architectures at each step can be followed in detail in the reported study. The symmetric supercapacitor device based on 3D G-MDHA (2D + 1D, \sim graphene + CNTs) electrode materials has displayed phenomenal areal capacitance (C_a) of $639.56 \text{ mF cm}^{-2}$ with capacitance retention up to 71.4% ($\sim 456.69 \text{ mF cm}^{-2}$) at 40 mA cm^{-2} . In comparison, a symmetric supercapacitor constituted on 3D GA electrode materials has contributed an areal capacitance of 262.7 mF cm^{-2} with capacitance retention up to 62.1% ($\sim 164.7 \text{ mF cm}^{-2}$). The improved rate capability of the device is mainly constituted by the intrinsic electrochemical contributions of multicomponent (graphene and CNTs) and unique printed architecture of MDHA. The 3D-printed well-interconnected hierarchical structure manifests unhampered pathways for the ion/electron transportation from the bottom to the peak surface of the graphene/MWCNT MDHA, maximizing its overall electrochemical contributions. Benefitting from the architecture of the 3D-printed MDHA, symmetric supercapacitor devices based on the various thickness ($\sim 0.5, 1, 1.5,$ and 2 mm) of electrode materials at different selected CDs (4 to 20 mA cm^{-2}) have also been well investigated. The

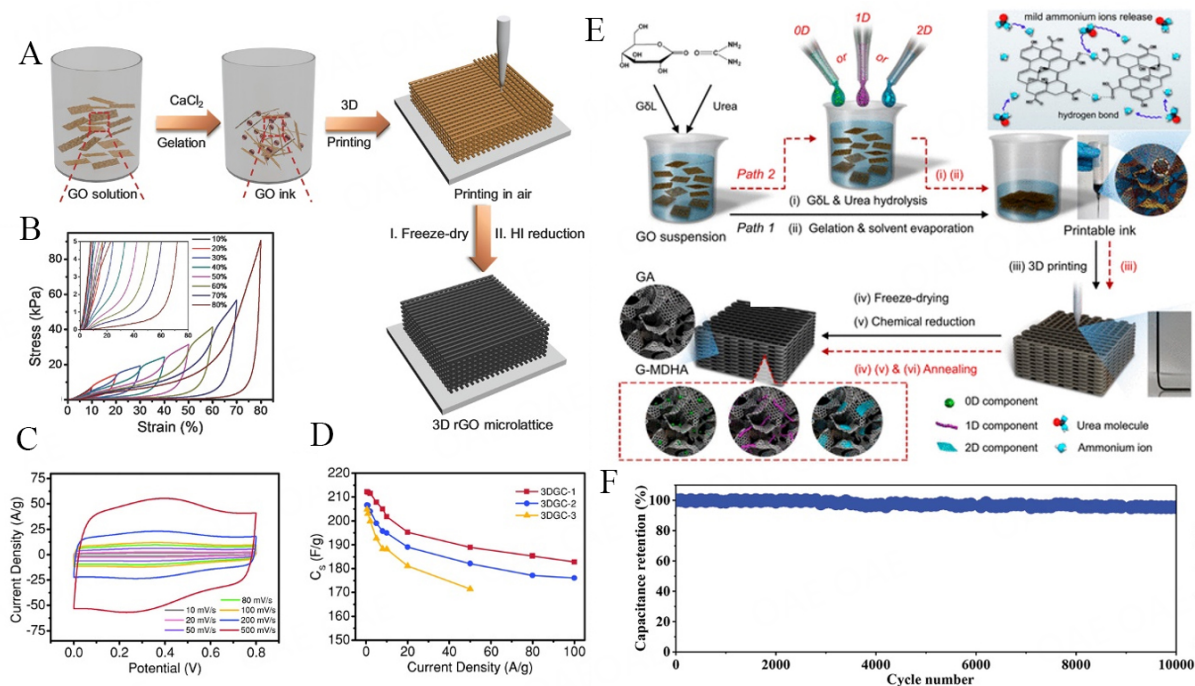


Figure 5. (A) Schematic presentation of 3D printing process guided through the provided arrows; initially, a certain quantity of CaCl_2 is inserted into GO solution to formulate GO ink inheriting appropriate rheological characteristics. In the next step, GO ink is squeezed out through a robot-controlled nozzle to develop 3D structure. Finally, the as-developed microlattices were properly freeze-dried to achieve solid graphene oxide (GO) aerogel, which is further reduced by HI to receive neat microlattices of graphene-printed aerogel; (B) the stress-strain curve for GO-driven microlattices; (C) CV curves of 3DGC-1 at varied scan-rate values; (D) rate-performance comparison for 3DGCs with various thickness^[95]; (E) schematic presentation of 3D-printed graphene aerogel (denoted as GA) and graphene-mixed-dimensional hybrid aerogel (denoted as G-MDHA); in reported path 1, urea and G δ L were mixed in the dilute GO suspension in order, accompanied by elevation of temperature to stimulate the gelation process assisted through controlled hydrolysis of urea during the evaporation of solvent (i and ii); subsequently the GO-driven ink was printed according to the designed architecture (iii); in the final step of path 1, the as-printed architecture was freeze-dried and chemically reduced to obtain graphene aerogel (iv and v). In route 2 of the same scheme, suspension based on multidimensional (e.g., 0D, 1D, and 2D) functional additives were added to the GO suspension, respectively, pursued by the identical treatment steps (i-v) adopted in step 1; finally extra annealing process (vi) was performed to develop G-MDHA^[85]; and (F) cycling stability of G-CNT printed composite electrode material at 0.10 mA cm^{-2} ^[91].

reported results illustrate that the areal-capacitance (C_a) of the device grows quasi-proportionally (\sim with slightly noticeable decay) as the electrode thickness/loadings increase, proposing that areal capacitance (C_a) can be further enhanced by enhancing the thickness of electrode materials. The variation in the CNTs contents (0, 2.5, 5, 10, 30, and 100 wt.%) on the graphene-driven printed electrode material has been well investigated by Wang *et al.*^[91]. They have concluded that 5 wt.% of CNTs is optimal content to attain improved electrochemical performance of the DIW-printed composite material [graphene-CNTs (G-CNTs)]. G-CNTs composite electrode material displayed a commendable areal capacitance value of 9.81 mF cm^{-2} at 0.05 mA cm^{-2} . Increase of CNTs contents beyond 5 wt.% was not beneficial in improving electrochemical performance of G-CNTs composite material as CNTs have lower charge storage capacity in comparison to graphene [which possesses a high SSA value ($315 \text{ m}^2 \text{ g}^{-1}$)]. The cycling stability contribution of optimized G-CNTs-5 sample was well investigated up to 10,000 cycles [Figure 5F]. It retained a phenomenal capacitance value of $\sim 95.5\%$. Hence, EDLC-driven architectures manufactured through the 3D DIW process possess highly porous structures and improved overall electrochemical performance. Moreover, the electrochemical performance of reported 2D materials for 3D-printed EDLCs has been well summarized in Supplementary Table 1.

2D materials for 3D-printed pseudocapacitors

Pseudocapacitors, a distinct subset within the realm of EESDs, have attracted substantial recognition due to their multifaceted advantages. These advantages originate from their unique electrochemical properties and structural characteristics, setting them apart from conventional capacitors and batteries^[96,97]. Unlike typical EDLCs, the energy in pseudocapacitors is stored through faradic reactions, in which ultrafast and reversible oxidation/reduction reactions take place near or at the electrode/electrolyte interface^[98-100]. Common 2D pseudocapacitive materials include conductive polymers, noble metals, metal oxides, and LDHs. As compared to EDLCs, 2D-driven pseudocapacitors have high potential to offer much more in terms of electrochemical contributions; however, their intrinsic electrochemical properties are mainly compromised due to their inferior electrical conductivity^[101-103]. Nevertheless, with the progress in advancing research, there has been rapid growth in emerging 2D pseudocapacitive materials, e.g., MXenes (metal carbides/nitrides), MOFs, transition metal oxides (TMOs)/hydroxides (HOs), LDHs, dichalcogenides, and black phosphorus (BP) with much improved electrochemical contributions^[104]. Considering the importance of advanced 2D materials, herein, we have disclosed and discussed the reported 3D-printed pseudocapacitors along with their key rheological, structural, and electrochemical characteristics. Huang *et al.* utilized MXene hydrogel for multi-scale structure engineering to fabricate supercapacitors^[105]. As depicted in [Figure 6A], they employed a method involving H₂SO₄ to facilitate the unidirectional growth of MXene and synthesize H₂SO₄-thawed MXene hydrogel. During the thawing process of freeze-dried MXene, it was revealed that the contact angle of water decreased due to the influence of H₂SO₄, leading to faster electrolyte penetration and improved rate performance. The MXene hydrogel film thus produced was used to create printed electrodes using the DIW method. When comparing the electrochemical properties of the produced MXene, disordered MXene, H₂SO₄-based aerogel, and filter-based film, it was found that the ordered MXene illustrated the highest overall capacitance of 393.0 F g⁻¹. Furthermore, it maintained a capacitance retention rate of 50% even when the scan rate elevated from minimum (100 mV s⁻¹) to maximum (1,000 mV s⁻¹) value, surpassing other electrodes by a significant margin [Figure 6B]. Additionally, it was determined that the R_{ct} (charge transfer resistance) value was exceptionally low. This group engineered MXene hydrogel through multi-scale structural control to create unidirectionally grown MXene hydrogel for the application of supercapacitors^[106]. They utilized 3D printing techniques to fabricate a honeycomb-like compartmentalized structure. This approach synergistically enhances the diffusion and mobility of electrolyte ions while increasing the available surface area for ion utilization. Zhou *et al.* used DIW technology to construct 3D architectures for EESDs, leveraging 2D MXene materials^[84]. Conventional techniques often struggle to achieve such complex structures. However, there is a challenge in meeting specific rheological characteristics for 3D printing process, as it necessitates a notable quantity of MXene in the ink. This, in turn, leads to a self-restacking structure issue after drying. To address this challenge, the research introduces a range of cellulose nanofibers (CNFs) with varying surface chemistries and morphologies. These CNFs are employed to enhance the rheological properties of the MXene-driven inks, ensuring phenomenal 3D printability of the mixture. The attained optimized hybrid ink, with a low solid content, successfully facilitates the printing of various 3D structures, maintaining superior shape preciseness and geometric accuracy. Upon freeze-drying, these 3D structures become self-standing and hierarchically porous. Shrinkage of MXene occurs during this process, and to minimize it, a method involving adding CNTs was employed. As seen in [Figure 6C], this approach effectively reduced the thickness from the initial 0.44 mm to 0.43 mm after freeze-drying. It was reported that this transformation can enhance ion transport efficiency, surface area accessibility, and pseudocapacitive performance. When comparing the capacitive and diffusive distribution using this approach, it was confirmed to have a capacitance distribution of 69.82% [Figure 6D]. Upon checking the galvanostatic charge-discharge (GCD) profiles, a high Coulombic efficiency (CE) was observed, and nonlinear data characteristic of a pseudocapacitor was evident [Figure 6E]. In particular, a solid-state interdigitated symmetrical supercapacitor (SSC) is 3D-printed, achieving notable results. It exhibits an areal capacitance value of 2.02 F cm⁻² with an ED of 101 μW h cm⁻². Even after 5,000

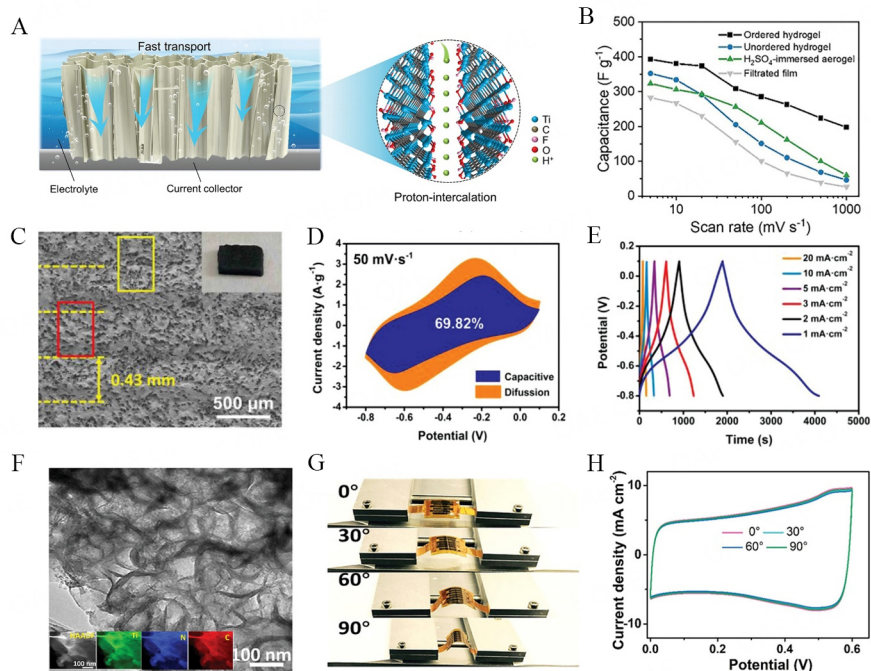


Figure 6. (A) Schematic illustration of MXene hydrogel supercapacitor electrode; (B) rate performance of the MXene hydrogel, unordered hydrogel, H_2SO_4 -immersed aerogel, and filtrated MXene film^[105]; (C) Top view SEM micro-structure of 3D-printed MXene; (D) CV graphs at 50 mV s^{-1} while the blue-colored area illustrating the surface capacitive contributions; (E) GCD graphs at different current density (CD) values^[84]; (F) TEM image of crumpled MXene-N nanosheets and HAADF-STEM elemental maps of N-doped MXene sheets; (G) digital photographs; and (H) CV graphs of N-doped MXene printed MSC under different bending angles^[107].

cycles, the device delivers a capacitance retention rate of 85%. The research conducted by Yu *et al.* has induced a practical approach to fabricating multifunctional systems with precisely designed architectures^[107]. In this context, 2D MXenes have gained considerable interest in the arena of printed energy storage devices. However, a significant challenge arises due to the van der Waals interaction between intrinsic MXene layers, leading to restacking problems within printed structures. These issues can substantially hinder ion and electrolyte transport, consequently affecting electrochemical performance. To address this challenge, the researchers demonstrate a melamine formaldehyde templating method to create crumpled nitrogen-doped MXene (N-MXene) nanosheets. The TEM observation in Figure 6F provides additional insights into the detailed structure of wrinkled N-MXene. Furthermore, HAADF-STEM images and the corresponding elemental mapping demonstrate the uniform distribution of native elements such as Ti, C, and N in the investigated area of doped-MXene. Nitrogen doping enhances electrochemical performance of MXene by improving redox activity and conductivity. Accordingly, two types of N-MXene inks are formulated, optimized for 2D screen printing and 3D extrusion printing processes. Doped-MXene displayed a pair of signature redox peaks relating to the protonation and change in the oxidation states of titanium atoms, indicating the typical pseudocapacitive behavior of MXene sheets. The screen-printed N-MXene MSC exhibits an areal capacitance value of 70.1 mF cm^{-2} while preserving excellent mechanical robustness. Moreover, the 3D-printed N-MXene-based supercapacitor, featuring a three-layered electrode, achieves an areal capacitance (C_a) of 8.2 F cm^{-2} and can store a high areal ED of $0.42 \text{ mW h cm}^{-2}$. Furthermore, this research team achieved enhanced flexibility performance through the 3D printing of pseudocapacitors. They conducted experiments by varying the bending angles, as shown in Figure 6G. During these experiments, it was confirmed that the shape of the CV curve remained unchanged, indicating excellent mechanical robustness [Figure 6H]. Moreover, these flexible cells also demonstrate a high cycle stability with a capacitance retention rate of 92% even after 7,000 cycles, showcasing their remarkable long-

term durability. Orangi *et al.* made self-powered and miniaturized energy storage devices that can contribute commendable power and energy densities within limited space availability^[108]. In this study, the researchers present a novel approach for the development of all-solid-state MSCs (SS-MSCs) using a 3D printing technique with the support of additive-free and water-driven MXene ink. The as-developed MSCs benefit significantly from the exceptional electrochemical properties and high electrical conductivity of $Ti_3C_2T_x$ materials. These materials, combined with a 3D interdigital electrode architecture, enable the MSCs to achieve remarkable volumetric and areal energy densities. The key innovation in this research study is the application of a highly-concentrated MXene ink with preferable viscoelastic characteristics, enabling extrusion printing process at room temperature. This approach facilitates scalable manufacturing of MSCs with various architecture designs and electrode thicknesses, even on a range of substrates, including flexible ones such as polymers and paper. The electrochemical outcome of the printed solid-state devices (PSSDs) was outstanding, with high C_a of up to approximately $1,035 \text{ mF cm}^{-2}$, showcasing their potential for sustainable energy storage applications. The innovative approach to harnessing versatile N-MXene inks provides profound intuition into the development of printed electrical equipment safety schemes (EESSs) characterized by high areal ED and scalability, paving the direction for the advancement of next-generation sustainable energy storage systems. Moreover, the key electrochemical performance of reported 2D materials for 3D-printed pseudocapacitors has been well summarized in [Supplementary Table 1](#).

2D materials for 3D-printed hybrid capacitors

Considering the individual electrochemical characteristics of EDLC- (high PD) and pseudocapacitor-driven (potential to deliver high ED) MSCs, their intrinsic lower energy contributions (~capacity to store energy per unit weight) are not up to the mark to consider them as alternatives to batteries at commercial scale^[109]. However, the combination of EDLCs and pseudocapacitive-driven materials, such as graphene, MXenes, TMDs, TMOs, LDHs, and MOFs in the hybrid form can deliver high ED without compromising the intrinsic high PD characteristics of supercapacitors. Hybrid capacitors employing 2D materials as active components are currently under active investigation. Utilizing 2D hybrid materials through advanced manufacturing process such as DIW 3D printing process, sustainable 3D architectures can be constructed [[Figure 7A](#)], possessing special characteristics such as high porosity, low density, and adjustable electrical conductivity. The integration of hybrid materials with the DIW method demonstrates superior capacitive performance compared to conventional bulk electrodes. Herein, their potential for application in microdevices through patterning has been revealed and discussed in detail. In the study by Zhao *et al.*, a highly electroactive Cu/Co-THQ@CNTs@GO (THQ: tetrahydroxy-1,4-quinone) microlattice electrode was applied to LIC (Lithium-ion Capacitor)^[110]. The electrodes were manufactured using 3D printing, with a diameter of approximately $250 \mu\text{m}$ and a center-to-center thickness of about $600 \mu\text{m}$, as depicted in [Figure 7B](#). The lamination process involved stacking the electrode layers from four to 16 layers. Upon investigation, it was observed that increasing the number of layers to 16 resulted in a lengthened electron transfer path, leading to a capacity decrease. The optimal thickness was found to be 12 layers, as shown in [Figure 7C](#). Beyond 12 layers, no significant difference in density was observed. To achieve high electrical conductivity, electrodes with a value of $0.41 \pm 0.07 \mu\text{S cm}^{-1}$ were fabricated. In this study, the researchers utilized Cu/Co-THQ@CNTs@GO as the cathode and vanadium nitride nanowire (VNNW)@ reduced GO (rGO) material as the anode, produced using 3D printing technique, to construct a hybrid supercapacitor. The resulting device exhibited remarkable capacity (178.68 F g^{-1}) and high ED ($396.89 \text{ W h kg}^{-1}$). The synergistic effect between 2D conductive MOF and 3D printing technology proved beneficial in enhancing the performance of hybrid supercapacitors. In the study by Yang *et al.*, quasi-2D materials derived from Kapok-driven roof tile-shaped Carbon tiles were utilized as electrode materials^[111]. The electrodes were fabricated using 3D printing to facilitate high mass loading and create channels for rapid ion diffusion. The resulting ink demonstrated non-Newtonian fluid behavior, covering a shear range from 10^{-2} to 10^{-3} s^{-1} . Analysis of the storage coefficient and loss coefficient revealed that the ink exhibited consistent loss

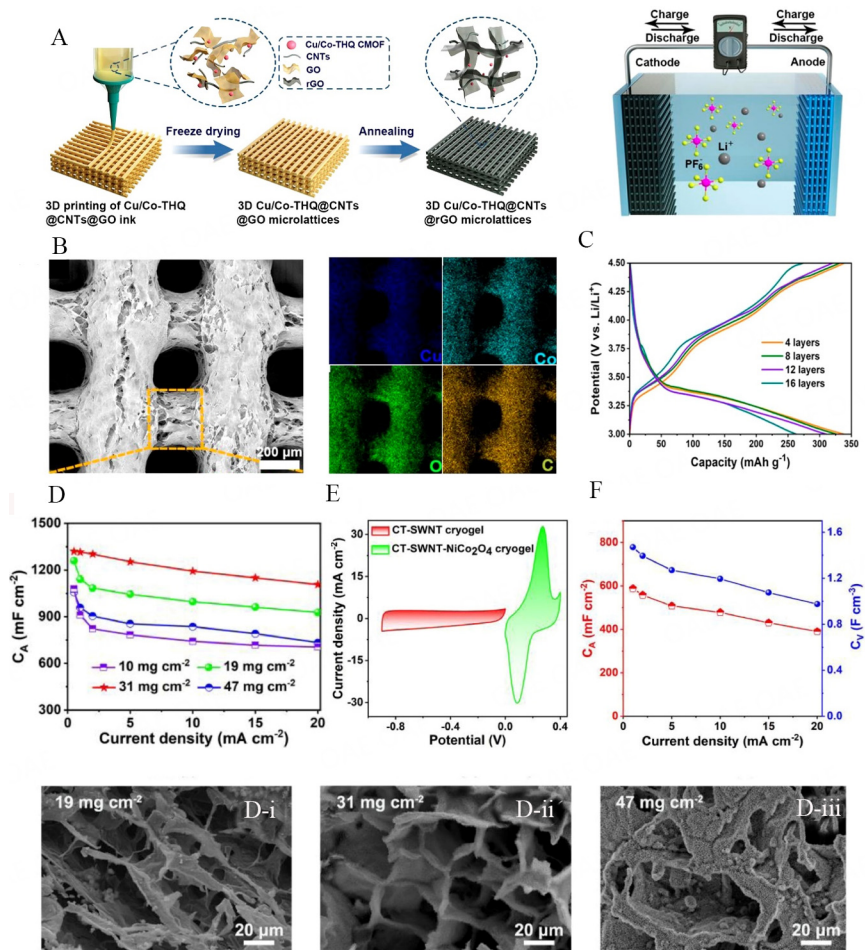


Figure 7. (A) Schematic illustration of making the 3D structure microlattices and hybrid capacitors; (B) SEM image of 3D structure electrode and SEM-EDX; (C) typical charging/discharging graphs of printed microlattices with various printed layers^[110]; (D) capacitance plots with different mass loadings^[111], (D-i-D-iii) microstructural analyses with the increase of NiCo₂O₄ content; (E) CV curve of hybrid-capacitor electrode; and (F) corresponding areal and volumetric capacitances at different current densities.

coefficients at low shear stress, indicating solid-like elastic properties below the flow point. The electrodes were constructed with dimensions of $10 \times 10 \times 5 \text{ mm}^3$ and displayed a remarkable ability to withstand compression without damage in over 50% of the samples. As a result, these electrodes achieved a high SSA of $1,253 \text{ m}^2 \text{ g}^{-1}$. This study conducted measurements while keeping the volume fixed and varying the capacity per unit area. When sample loading exceeded 30 mg cm^{-2} , excessive pores were blocked [Figure 7D(D-i-D-iii)], and the sample occupied free space, leading to hindered ion diffusion, and reduced electrochemical performance [Figure 7D]. Using optimized samples, the researchers fabricated a hybrid capacitor by employing CT-SWNT-NiCo₂O₄ as the cathode and 3D-structured CT-SWNT-NiCo₂O₄ as the anode materials [Figure 7E]. In the existence of reported electrode materials, respective research group achieved high areal and volumetric capacitance values [Figure 7F], highlighting the potential of 3D printing approaches for enhancing hybrid capacitor performance. One such method, described by Zhao *et al.*, outlines the process of constructing hybrid aerogel microlattices using 2D complexes through 3D printing technology^[112]. This approach aims to achieve improved cost efficiency and cycling performance^[113]. Zhou *et al.* employed DIW to print 2D pseudocapacitive materials, specifically MXene, known for its exceptional properties^[84]. However, they faced a significant challenge with severe MXene restacking during printing. To address this, they incorporated 2D capacitive material, CNFs, to improve the rheological properties of

MXene-based ink, leading to improved 3D printability. By adjusting the content of 1D CNF in 2D MXene and adding 10 wt.% CNF, they observed excellent shear-thinning behavior, high G' (storage modulus), and remarkable yield stress, indicating superior 3D printability. The resulting samples were utilized in energy storage devices, exhibiting a high areal capacity of 2.02 F cm^{-2} and phenomenal cycling stability. Zhao *et al.* successfully developed a novel DIW printing material by combining 2D layered GO, 1D capacitive material (MWCNT), and 1D pseudocapacitive material (KCu_7S_4)^[114]. They fabricated electrodes through freeze-drying and chemical reduction after printing, resulting in a conductive bridging structure formed through self-assembly. The eight-layer DIW-printed electrodes exhibited impressive electrochemical performance, achieving an areal capacity of 27.8 F cm^{-2} and a volumetric capacity of 73.1 F cm^{-3} . Moreover, after the completion of 2,000 cycles, they demonstrated an exceptional capacity retention rate of 88.6%. The strategic combination of 2D GO, 1D MWCNT, and 1D KCu_7S_4 in a DIW printing material opens new possibilities for enhancing capacitance and cycling stability, paving the channel for next-generation sustainable energy storage systems. Across the hybrid-capacitor domain, 3D printing technology is gaining significant attention due to its potential to create structures with high SSAs, porosity, and excellent electrical conductivity. This growing interest reflects the ongoing pursuit of innovative approaches to boost the performance of MSCs. The electrochemical contributions of reported 2D materials for 3D-printed hybrid capacitors are illustrated in [Supplementary Table 1](#).

2D MATERIALS FOR 3D DIW-PRINTED MICRO-BATTERIES

2D materials for 3D-printed Li-based batteries

Li-based batteries have presented themselves as potential candidates to empower electric vehicles or portable gadgets owing to their high ED and lengthy cyclic life contributions^[115-117]. However, commercially available Li-based batteries also display confined electrochemical outcomes mainly due to the application of conventional electroactive materials and their basic reported geometries such as pouch cells, prismatic, coin, and cylinder. To develop high-rated Li-driven batteries, application of advanced electroactive materials, proper design, and manufacturing process of various battery modules such as anodes/ cathodes, separators, and electrolytes can play significant roles^[60]. In this regard, development of Li-based batteries based on 2D electroactive materials through advanced manufacturing processes such as DIW printing process is heavily under investigation^[118]. This unique combination has resulted in the formation of well-patterned microstructures for Li-driven batteries with sustainable electrochemical contributions to meet the advanced energy storage milestones. The key factors which help to attain such prominent electrochemical performance are outlined as follows; (i) 3D printing process enables the deposition of high areal mass loadings of electroactive materials; (ii) availability of shorter ion-diffusion pathways in the printed architecture; (iii) formation of sufficiently deep porous architectures, facilitating the storage of electrolyte solution during redox process proceedings; (iv) providing opportunity to fabricated complex printed architectures with required design and dimensions; and (v) 2D materials physical/chemical characteristics help to develop mechanically sustainable 3D architectures^[119-121]. Regarding the formation of 3D-printed architectures based on 2D materials, various studies, along with their key results and findings, have been disclosed and summarized as follows. Sun *et al.* have mixed rGO, silver nanowires (AgNWs) and lithium tin oxide (LTO) to fabricate thick-electrode material demonstrating phenomenal areal capacity value and rate performance for 3D-printed lithium-ion batteries^[122]. They control the areal capacity contributions of the reported electrode material with the number of its deposited ink layers (thickness ranging from 150 to 1,500 μm). Benefitting from a highly conductive AgNW network embedded in the 3D-printed graphene scaffold structure, they reported a high areal capacity value of up to 4.74 mAh cm^{-2} with a maximum electrode thickness of 1,500 μm (~ 10 deposited layers) [[Figure 8A](#)]. In comparison, rGO-LTO binary 3D-printed composite electrode material can display only half of the areal capacity value with a maximum electrode thickness of 900 μm . Graphical presentation of electron and ion transportation kinetics occurring in the 3D-printed architecture of rGO-AgNWs-LTO-driven electrode is displayed in [Figure 8A\(A-i\)](#) and is described

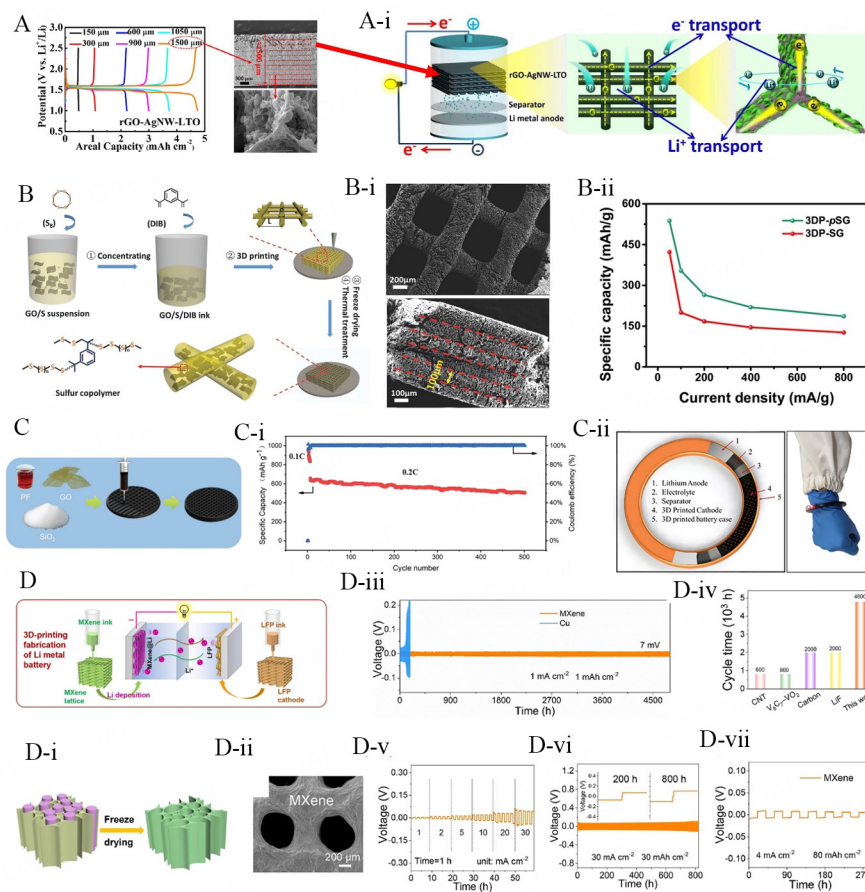


Figure 8. (A) Gel-based thick electrode fabrication mixing with 2D materials realization of high mass loading electrode^[122]; (A-i) graphical presentation of the electrons and ions movement behavior in 3D-printed rGO-AgNWs-LTO electrodes and discharging process of respective material for lithium metal battery system; (B) schematic diagram of lithium sulfur copolymer for 3D printing^[124]; (B-i) SEM microstructure of 3DP-pSG architecture from top; (B-ii) lateral view of the architecture disclosing layer-by-layer deposition of stacked filaments; (C) schematic diagram of 3D printing architecture for high loading lithium sulfur battery^[125]; (C-i) cycling contributions of Li-S coin cell assembled through 3D-PC with maximum sulfur areal loadings of 10.2 mg cm⁻² at 0.2 C; (C-ii) assembly illustration of bracelet-like battery; (D) schematic presentation of 3D printing process of LFP and MXene ink for lithium metal batteries^[127]; (D-i) schematic presentation of freeze-drying process for the development of porous MXene microlattices; (D-ii) top-view of the as-developed porous MXene lattices; (D-iii) cycling life contributions of MXene@Li and Cu@Li anodes-driven symmetric cells (SCs) with a plating/stripping capacity of 1 mAh cm⁻² at 1 mA cm⁻²; (D-iv) cycling life comparison of MXene@Li electrode with earlier documented 3D-printed architectures deployed for lithium metal anodes (LMA) at 1 mA cm⁻²; (D-v) rate-capability contributions of MXene@Li-based symmetric-cell (evaluated from 1 to 30 mA cm⁻² for 60 min); (d-vi) cycle time of symmetric cell MXene@Li cells at 30 mA cm⁻² and areal capacity of 30 mAh cm⁻²; and (D-vii) the areal capacity of 80 mAh cm⁻² at 4 mA cm⁻².

through the following enlisted points. Firstly, the open mesh architecture (~250 sufficiently widely square pores) and ample micropores in the printed filaments provide access to the liquid and electrolyte to the inner active electroactive sites and also act as a reservoir to locally stock the electrolyte solution. The presence of stored electrolyte solution ensures a stable electrochemically active environment for the lithium-ion transportation during the charging/discharging cycles. Secondly, the existence of AgNWs in the 3D-printed architecture tightly encloses the LTO nanoparticles, which facilitates the quick transmission of electrons from the core to the outer edge, even in thick electrode materials up to 1,500 μm. Lastly, dynamic graphene has contributed multifunctionally by providing sufficient conductivity, mechanical strength, and toughness, which are important factors from an electrode sustainability point of view. Thus, owing to the existence of synergistic effect among all multi-materials of the system, the maximum thickness of the electrode material was attained, which helped to improve its rate performance and areal capacity

contributions.

In order to fulfill the high ED demands for the development of modern wearable microelectronic and electric vehicle systems, conventional lithium-ion batteries are being replaced by other efficient systems such as Li-sulfur (S), Li-air, and lithium metal batteries (LMBs). Herein, considering the importance of these advanced systems, we have discussed the prominent studies covering the core subject of this review article. In comparison to conventional lithium-ion batteries, LMBs based on sulfur cathode materials possess excellent theoretical ED up to 2,600 Wh kg⁻¹[123]. Moreover, sulfur also exists abundantly in nature and is atmosphere-friendly. In this regard, 3D sulfur copolymer-graphene architectures (3DP-*p*SG) with well-arranged microlattices have been reported by Shen *et al.* for Li-S batteries. Process involved in the development of 3D-printed sulfur copolymer-graphene (3DP-*p*SG) architectures is well-illustrated in Figure 8B^[124]. After the preparation of GO/S/DIB-driven ink, it was poured into a 3 mL syringe to initiate a printing process of layered-by-layered architectures. In the final prominent synthesis step, the sulfur copolymer was grown on the graphene nanosheets by exposing the 3D-printed architecture to 200 °C for a specific reaction of time. The SEM microstructures of (3DP-*p*SG) architecture covering its top and lateral views are displayed in Figure 8B(B-i). Top-view of the 3DP-*p*SG architecture clearly illustrates the existence of well-defined macropores, which were developed from continuous filaments with an average diameter of 200 μm. Moreover, top-view analysis also confirms the structural coherence of the 3D-printed architecture despite the fact that it was exposed to a thermal treatment. The lateral view of the architecture demonstrates the existence of well-diffused six printed layers with a constant thickness of 100 μm for each layer, facilitating sustainable mechanical stability to the whole architecture. In comparison to 3DP-SG (specific capacity value ~680.7 mA h g⁻¹), the 3DP-*p*SG architecture has contributed a phenomenal specific capacity value of 812.8 mA h g⁻¹. Moreover, with the increase of CD from minimum to maximum values (~50 to 800 mA h g⁻¹), the 3DP-*p*SG architecture maintains a noticeable reversible capacity value of 186 mA h g⁻¹ in comparison to 3DP-SG (126 mA h g⁻¹) at the same CD value [Figure 8B(B-ii)]. The obtained superior electrochemical contributions of 3DP-*p*SG architecture are associated with the presence of sulfur copolymer, which has suppressed the dissolution of polysulfides into the electrolyte solution owing to the presence of a strong covalent bond between C-S. Noticing the importance of Li-S batteries, Chen *et al.* have also fabricated high loading ones for wearable applications by a 3D printing process^[125]. The adopted protocol to synthesize the 3D-printed cathode (3D-PC) is schematically illustrated in Figure 8C. Briefly, selected amounts of GO (80 mg) and SiO₂ (400 mg) were initially sonicated in a certain volume (2 mL) of water for particular time (12 h), and then a certain amount (800 mg) of phenol formaldehyde (PF) resin was included and the whole mixture was stirred for another 12 h to attain a thick paste. The as-obtained thick paste was inserted into the syringe for a 3D printing process, where 3D cathode material was printed through a nozzle of 150 μm, under controlled printing speed and driving pressure of 5 mm s⁻¹ and 6.5 bar, respectively. After completing the 3D printing process, the printed cathode material was properly dried for 1 h at 80 °C. Next, the 3D-PC was treated under nitrogen atmosphere at 1,000 °C for 12 h; then, it was etched with the aid of hydrofluoric acid for particular time of 12 h in order to detach the SiO₂ particles. Finally, the 3D-PC was soaked into S/CS₂ solution for 5 min and then was heated for 12 h at 150 °C. Owing to the highly conductive 3D skeleton structure with interpenetrating-transmission channels for ions and electrons, the as-developed 3D Li-S battery has displayed phenomenal specific capacity value of 505.4 mA h g⁻¹ after the completion of 500 cycles, with maximum active material loadings of 10.2 mg cm⁻² [Figure 8C(C-i)]. The unique aspect of this study is that it has reported the development of 3D-printed wearable Li-S bracelet-type batteries. In detail, the as-obtained 3D-PC was constructed with Li-driven anode material, separated by a separator (~Celgard 2,500) into a well-drafted 3D-printed case, as illustrated in Figure 8C(C-ii). The successful development of bracelet-like batteries was confirmed by connecting two LEDs, which successfully glowed, as displayed in Figure 8C(C-ii).

Other prominent systems that have the capacity to replace traditional lithium-ion anode materials (e.g., graphite, which owns a maximum theoretical specific capacity value of $\sim 372 \text{ mA h g}^{-1}$) are lithium metal-driven anode materials with an ultrahigh theoretical specific capacity value of $\sim 3,860 \text{ mA h g}^{-1}$ and very low redox potential [-3.040 V vs. SHE (standard hydrogen electrode)]^[126]. However, several hurdles should be properly addressed prior to the utilization of lithium metal-driven anode materials for rechargeable LMBs, e.g., (i) uncontrollable growth of Li dendrites, which can raise various safety issues; (ii) generation of thick solid electrolyte interphase (SEI) on the lithium metal surface, resulting in maximum internal charge resistance; and (iii) large morphological and volumetric changes can take place in lithium metal anodes during repeated number of plating and stripping cycles. In order to control the aforementioned issues, Ma *et al.* have reported the deposition of MXene as a protective layer for copper current collectors by 3D printing MXene^[127]. The detailed adopted protocol for manufacturing 3D-printed LMBs is schematically disclosed in [Figure 8D](#). MXene ink was successfully deposited layer-by-layer on Cu foil via extrusion-driven printing process (DIW). Subsequently, freeze-drying process resulted in the formation of a 3D porous network in the printed MXene architecture, caused by the perpendicular growth of ice crystals to the utilized substrate [[Figure 8D\(D-i\)](#)]. Furthermore, the FE-SEM microstructure of the 3D-printed MXene architecture also confirms the existence of its regular macro-sized holes and parallel vertical pores throughout the entire printed lattice [[Figure 8D\(D-ii\)](#)]. Such hierarchically structured and well-ordered 3D porous architecture will not only ensure the fast ion/electron transmission and adequate electrolyte solution infiltration but also shield the volume expansion of lithium metal, favoring the deposition of higher Li contents. The adopted strategy has also been well translated into the phenomenal electrochemical contributions displayed by the 3D-printed MXene lattice [[Figure 8D\(D-iii\)](#)]. In detail, the MXene@Li and plain Li foils-driven symmetric cells were assembled to analyze their cycling stability and Li plating/stripping behaviors. The MXene@Li symmetric cell demonstrated consistently firm voltage profiles with a marginal overpotential value of approximately 7 mV after cycling it continuously for over 4,800 h, while, on the other hand, plain Cu-driven symmetric cell had swift voltage changes and sharp rising voltage hysteresis after just 95 h, as the stability cycles progress, a significant overpotential value of 0.2 V has been reported after 150 h at a deposition capacity of 1 mA h cm^{-2} at 1 mA cm^{-2} . The reported ultralong cycling life of MXene@Li symmetric cell is far better in comparison to previously documented 3D-printed Li anodes, e.g., LiF (2,000 h)^[128], N-doped carbon (2,000 h)^[129], CNT (800 h)^[130], and $\text{V}_8\text{C}_7\text{-VO}_2$ (800 h)^[131] [[Figure 8D\(D-iv\)](#)]. Moreover, as the CD value was systematically augmented (from 1 to 30 mA cm^{-2}) followed by the stripping/plating capacities ranging from 1 to 30 mAh cm^{-2} , the overpotential value increased significantly (from 4 to 45 mV) [[Figure 8D\(D-v\)](#)], indicating the excellent rate-capability performance of the manufactured MXene@Li symmetric cell. Notably, a stable overpotential was also recorded for MXene@Li symmetric cell for certain cycles (800) at 30 mA cm^{-2} and capacity of 30 mAh cm^{-2} [[Figure 8D\(D-vi\)](#)], confirming the outstanding characteristics of MXene-driven printed lattices as sustainable Li anodes with minimum and constant voltage hysteresis. To further investigate the advantages of 3D-printed thick MXene microelectrodes as stable platforms for Li, an ultra-high Li stripping/plating capacity of 80 mAh cm^{-2} at 4 mA cm^{-2} was performed, wherein the attained MXene@Li manifested voltage contours with an overpotential value of only 8 mV for over 280 h [as displayed in [Figure 8D\(D-vii\)](#)], supporting the suitability of developed high ED LMBs. The electrochemical contributions of reported 2D materials for 3D-printed Li-based batteries are demonstrated in [Supplementary Table 2](#).

2D materials for 3D-printed next-generation batteries

Extensive research is under progress on next-generation batteries (such as zinc-ion batteries, sodium-ion batteries, and vanadium redox flow (VRF) batteries) to present them as an alternative to the Li-based batteries^[132]. There are various advantages associated with such batteries. For instance, sodium-ion batteries have the potential to replace lithium batteries owing to high abundance of sodium (\sim the 4th most excessive element in the earth's crust)^[133,134]; likewise, zinc-ion batteries and VRF batteries have also presented

themselves as potential contenders in electrochemical energy storage systems owing to their low price, inherent protection, rich reserves, and eco-friendly-mode, safe in operations and ultra-long cycling life contributions, respectively^[135-137]. The exploration of the advantages offered by 2D materials in next-generation 3D-printed batteries illuminates their transformative potential in energy storage applications. With enhanced electrical conductivity, superior electrochemical performance, mechanical flexibility, and materials diversification capabilities^[138], the findings from this study underscore the significance of ongoing research and development efforts aimed at fully harnessing the potential of 2D materials, driving the progress of sustainable and high-performance energy storage solutions for the future^[139]. Wang *et al.* made significant strides by harnessing state-of-the-art 3D printing technology to create $V_2CT_x/rGO-CNT$ MXene microgrid aerogels, which serve as a highly promising matrix for sodium metal anodes [Figure 9A]^[140]. The intricate 3D-printed microgrid structures offer a hierarchical porous framework that not only ensures the utmost stability of the whole electrode during repetitive plating and stripping processes but also facilitates a vast surface area. This expanded surface area aids in reducing the CD and offers numerous active sites, fostering efficient sodium metal nucleation. *In-situ* transmission electron microscopy (TEM) characterization on $V_2CT_x/rGO-CNT$ electrodes to delve deeper into the intriguing phenomenon of sodium metal deposition. This analytical approach was compared with the selected area electron diffraction (SAED) pattern after sodium deposition [Figure 9B]. It reveals the diffraction patterns of Na_2O and $NaOH$. The emergence of these new patterns strongly suggests an intricate interaction between sodium and the V_2CT_x surface functional groups ($=O$ and $-OH$), leading to the formation of inorganic compounds, Na_2O and $NaOH$. This intriguing finding provides valuable insights into the complex chemical transformations occurring at the V_2CT_x surface during the sodium deposition process. The current study highlights the advancements made with the 3D-printed $V_2CT_x/rGO-CNT$ electrode, which is comprehensively compared to different MXene-driven sodium metal electrodes and 3D-printed sodium metal electrode architectures in terms of electrochemical performance [Figure 9C]. Remarkably, the 3D-printed $V_2CT_x/rGO-CNT$ electrode exhibits exceptional long cycle life, particularly under high CDs and large areal capacities, extending up to 50 mA h cm^{-2} . This remarkable finding emphasizes the recognition of the application of 2D materials in 3D printing for next-generation batteries. Li *et al.* have successfully synthesized a composite electrode comprising rGO and Super-P aerogel for VRF batteries [Figure 9D]^[141]. This electrode exhibits a controllable porous structure and was created using the DIW printing technique. The uniform distribution of Super-P on rGO sheets is believed to contribute significantly to the improvement of electrode performances. The voltage efficiency (VE) and CE variations for cells incorporating different materials [e.g., rGO, graphite felt (GF), rGO + COOH-MWCNT, rGO + CNF, and rGO-P] have been tested up to 100 cycles [Figure 9E]. All cells demonstrate CE values exceeding 95%, indicating excellent airtightness primarily due to the protective properties of the anolyte in a nitrogen atmosphere. Furthermore, the energy efficiency (EE) of each electrode was tested at CD values in the range of 80 to 160 mA cm^{-2} [Figure 9F]. With an incline in CD value, the energy efficiencies of all samples decline due to the effect of increased polarization. More specifically, as the CD increases, the EE of rGO-P is observed to be 70.75%, 64.26%, 59.39%, 55.04%, and 50.70%, respectively. Importantly, among all the aerogel samples, the cell equipped with rGO-P demonstrates the most favorable rate performance, being only slightly inferior to the cell using GF.

As explained earlier comprehensively about the importance of ZIBs, in this regard, Ma *et al.* have managed to attain improved performance of 3D printable ink, which was comprised of iron vanadate and reduced holey GO (rHGO). It is noteworthy that cellular cathode material with hierarchical porous structure for aqueous ZIBs was designed and manufactured by 3D printing process for the very first time^[142]. To elucidate the electrochemical reactions occurring during the charging and discharging of 3DP-FeVO/rHGO cathodes, ex-situ X-ray Photoelectron Spectroscopy (XPS) of Vanadium (V) and Iron (Fe) at three distinct stages: the initial state, the discharged state (0.4 V), and the charged state (1.6 V) for the first cycle were performed [Figure 9G and H]. In the discharged state, a reduction in the intensity of the V^{5+} peak and an increase in the

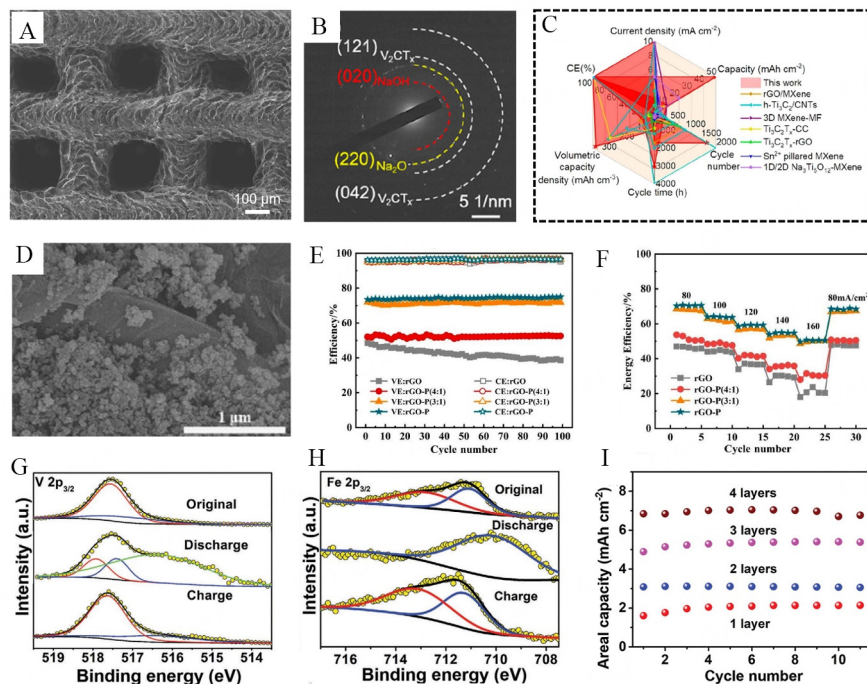


Figure 9. (A) SEM image of the 30% $V_2CT_x/rGO-CNT$ microgrid aerogel; (B) SAED patterns of $V_2CT_x/rGO-CNT$ after sodium deposition; (C) radar-charts illustrating electrochemical performance comparison of various MXene-based sodium metal anodes^[140]; (D) SEM surface morphology of rGO-P; (E) VE and CE of cells (with rGO, rGO-P (4:1), rGO-P (3:1) and rGO-P) at 80 mA cm^{-2} ; (F) energy efficiency (EE) curves at various current density values^[141], XPS spectra of 3DP-FeVO/rHGO cathodes for (G) $V 2p_{3/2}$ and (H) $Fe 2p_{3/2}$; and (I) areal capacities of 3DP-FeVO/rHGO with varied number of printing-layers (at 6 mA cm^{-2})^[142].

intensity of the V^{4+} peak was observed for $V2p_{3/2}$ spectra. Additionally, a novel peak at approximately 516.4 eV corresponding to V^{3+} emerged with a relatively higher intensity than that of the V^{4+} peak. In the charged state, both V^{3+} and V^{4+} species were observed to undergo oxidation, leading to the regeneration of V^{5+} . A similar phenomenon was observed in the $Fe 2p_{3/2}$ spectra, wherein Fe^{3+} underwent reduction during the discharge process, and the $Fe 2p_{3/2}$ spectra returned to their original state following the charging process. These results indicate a notable degree of reversibility in the transformations of both the V and Fe elements throughout the cycling process. Moreover, experiments involving an increase in the number of printing layers of 3DP-FeVO/rHGO cathodes were conducted to illustrate the practical benefits on mass loading [Figure 9I]. At heightened mass loading level, the areal capacity contribution by 3DP-FeVO/rHGO cathode material reached an impressive value of 7.04 mAh cm^{-2} at CD of 6 mA cm^{-2} . The results confirm that using the versatile DIW-driven 3D printing technique can attain phenomenal areal specific capacity for microelectrodes and an exceptionally elevated volumetric ED (VED) for zinc-ion batteries. Impacts of doping on the uniform deposition of Na have been studied in detail by Yang *et al.*^[143]. They developed a 3D-printed microlattice host composed of nitrogen-doped graphene aerogel (3DP-NGA) to precisely control the uniform nucleation and deposition of Na [Figure 10A]. Through density functional theory (DFT) calculations, the affinity of Na with three distinct N-doping sites was investigated [Figure 10B]. The findings unveiled binding energies of approximately 1.478, 1.537, and 0.561 eV for pyrrolic-N, pyridinic-N, and graphitic-N, respectively, when in contact with sodium metal [Figure 10C]. Remarkably, these binding energies are significantly higher than the binding energy observed between graphene and sodium metal, which stands at approximately 0.059 eV. The predominant influence of higher binding energy, primarily linked to pyrrolic-N, plays a central role in diminishing the nucleation barrier for sodium metal. Consequently, this effect results in the successful avoidance of dendrite formation during deposition and

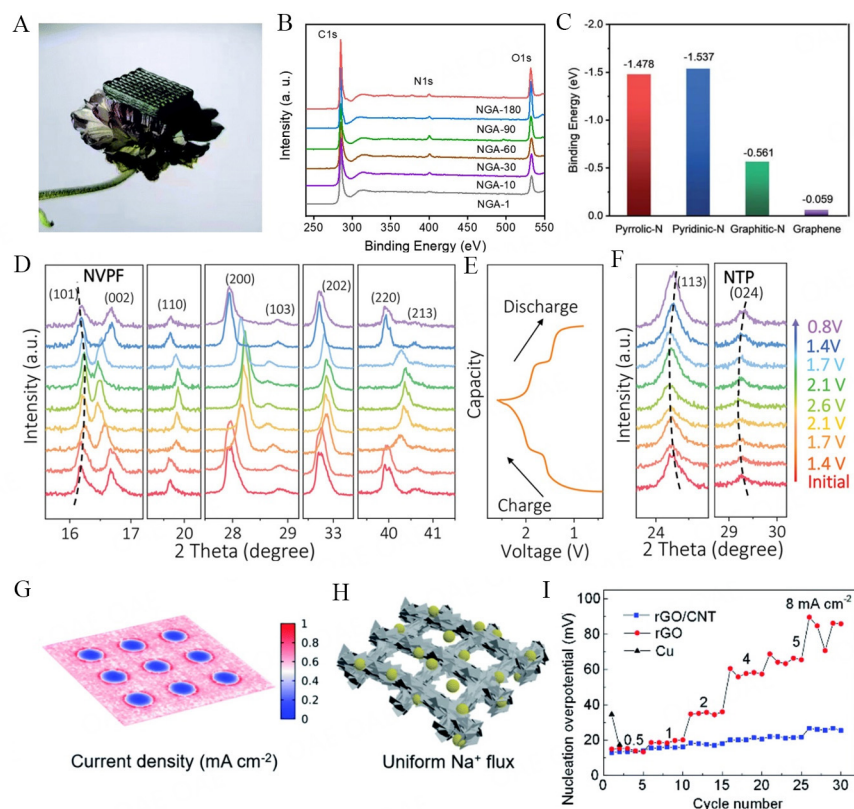


Figure 10. (A) Digital photo illustration of the 3D-printed rGO aerogel microelectrode placed on a flower; (B) XPS full spectrum of the 3DP-NGA with various N₂ plasma treatment durations; (C) binding energies of Na atoms with pyridinic-N, pyrrolic-N, graphitic-N, and graphene by DFT calculations^[143]; (D) *ex-situ* XRD spectrums of NVPF cathode material evaluated at various voltages; (E) GCD graphs reported at 1 C, (F) *ex-situ* XRD spectrums of NTP anode material attained at various voltages^[144]; (G) simulation model of the current density (CD) dispersal on the surface of the 3D-printed rGO/CNT porous microlattice aerogel (p-MLA); (H) schematic presentation of Na nucleation/plating behavior on printed rGO/CNT microlattice aerogel; and (I) nucleation overpotentials of the electrodes at different CD values^[145].

greatly advances the creation of high-performance sodium metal anodes. Moreover, the proportions of each N-configuration following various durations of plasma treatment were further examined. Notably, with the extension of plasma treatment time, the pyrrolic-N proportion increases while the graphitic-N proportion decreases. This observation suggests that the ratio between pyrrolic-N and graphitic-N can be effectively controlled by altering the duration of the plasma treatment which could be the pivotal factor in harnessing the optimal performance of the electrode.

To meet the advanced requirements of the fast-growing miniaturization industry, researchers/scientists are always on the move to design and fabricate novel 3D-printed energy storage systems to attain the required results. In this regard, Ma *et al.* have achieved a significant milestone by successfully creating fully 3D-printed flexible interdigital sodium-ion MBs (NIMBs) that incorporate a comprehensive 3D conductive carrier-transfer network^[144]. This pioneering accomplishment represents the first instance of such a construction and highlights a remarkable improvement in both areal and volumetric capacity, along with enhanced rate capability. They formulated 3D-printed microelectrode inks with Na₃V₂(PO₄)₂O₂F (NVPF) or NaTi₂(PO₄)₃ (NTP), which were enriched owing to the existence of highly conductive additives such as 1D CNTs and 2D electrochemically exfoliated graphene (EG) nanosheets. Furthermore, *ex-situ* X-ray diffraction (XRD) patterns were used to probe the structural changes in the NVPF cathode and NTP anode during cycles [Figure 10D]. In charging process of the NVPF cathode, the (200) plane diffraction peak at

27.93° gradually transferred to higher angles and eventually vanished by the end of the low charge plateau (~1.85 V). Simultaneously, a new peak emerged at 28.14°. This shift and emergence indicated a transformation from NVPF to $\text{Na}_2\text{V}_2(\text{PO}_4)_2\text{O}_2\text{F}$, correlating to the desodiation process during the low plateau. As the charge plateau increased (1.95 V), the newly formed peak at 28.14° continued to shift to even higher angles. Similar trends were observed for other diffraction peaks, indicating a two-phase transformation. The NTP anode experienced minor interlayer spacing expansion during charging [Figure 10E], as indicated by the gradual shifts in its diffraction peaks. During discharging, both the cathode and anode diffraction peaks reverted to their initial conditions, highlighting the highly reversible nature of the sodium-ion intercalation and deintercalation reactions in the NIMB [Figure 10F]. This high reversibility in structural changes during the sodium-ion insertion/extraction process contributes to microelectrode stability and extends the battery lifespan. Yan *et al.* reported a straightforward technique for creating a microlattice aerogel using 3D printing technology^[145]. This approach utilized rGO and CNTs (rGO/CNT) to produce a hierarchical periodic microlattice with submillimeter-sized filaments and channels, along with micrometer-scale pores, all of which could be tailored to specific thicknesses. CD distribution of 3D rGO/CNT was investigated to explore the benefits of the printed structure [Figure 10G]. According to the result, uniformly distributed CD was observed compared to modified planar copper foil. Therefore, sodium ions are evenly distributed throughout the entire 3D rGO/CNT microlattice aerogel. This uniform distribution is made possible by the substantial surface area value of the rGO/CNTs, which measures $414.6 \text{ cm}^2 \text{ g}^{-1}$, exceeding that of planar Cu foil. As a result, the local CD decreases significantly, leading to an extended Sand's time. Consequently, sodium metal nucleation and deposition within the 3D rGO/CNT matrix become more uniform while maintaining a stable SEI film [Figure 10H]. Nucleation overpotentials of the as-developed electrodes at different CDs were examined to compare the practical rate-capability of rGO/CNT microlattice aerogels [Figure 10I]. Certainly, the meticulously designed hierarchical structure is the key contributor to the exceptional rate-capability of the Na@rGO/CNT microlattice anode. This structure ensures remarkable electron conductivity and rapid ion transport speed, collectively resulting in its outstanding performance. The electrochemical performance of reported 2D materials for 3D-printed next-generation batteries is disclosed in [Supplementary Table 2](#).

CONCLUSIONS AND PERSPECTIVES

Sustainable 3D architectures with complex structures cannot be produced via ordinary dimensional materials and conventional manufacturing techniques. However, with the aid of 2D materials, advanced printing technologies possess recognizable potential to fabricate miniaturized EESDs to meet the requirements of the fast-growing electronics industry. Herein, after a brief introduction of 3D printing process, first, we summarized various 3D printing technologies along with their key advantages and disadvantages, followed by emphasizing extrusion-based DIW process and rheological characteristics of 2D materials-driven inks. From a rheological characteristics point of view, the printing inks with higher elastic modulus ($G'/G'' > 1$) can be appropriate for 3D DIW printing process. In this regard, binder-free modern materials, such as MXene, can help attain optimum viscoelastic behavior with moderate concentrations, mainly owing to their high aspect ratio (~4,000). Moreover, other key parameters disclosing the unique relationship between 2D materials and DIW printing process for the development of high-performance MEESDs have also been disclosed in detail. Additionally, 2D materials-driven 3D-printed architectures contribute unique characteristics which are summarized through the following discussed multiple points: (i) such architectures possess large SSA and enriched surface redox contributions; (ii) highly functional 2D inks with increased material loadings possess appropriate viscoelastic behavior to support the sustainability of 3D complex architectures; (iii) open mesh printed architecture (~250 sufficiently widely square pores) with existence of abundant micropores provides access to the electrolyte to the inner active electroactive sites and also acts as a reservoir to locally stock the electrolyte solution; (iv) 2D materials-driven building

blocks support the development of high-performance hierarchically structured microelectrodes; and (v) freedom to design architectures of required size/dimensions with HR impacts. Thus, in the essence of the aforementioned discussion, we have reviewed in detail the recent developments and adopted research procedures deployed to construct 2D materials-driven DIW-printed MEESDs. The reported MSCs and MBs have shown high specific capacitance/capacity, improved rate-capability, wide operating voltage, enhanced ED and PD, and longer cycling stabilities.

Considering the particular subject of the current study, promising developments have been reported with exciting results; however, this research topic remains in the early stages of evolution, and several prominent challenges exist and are suggested to be pondered in the future.

- Inactive binders or additives can restrict and deteriorate electrochemical performance of MEESDs, so immense efforts should be devoted to designing and applying advanced additive-free electroactive materials such as 2D MXenes. Such materials with excellent electrical conductivity, good rheological characteristics, and enriched redox contributions are highly recommended to develop sustainable miniaturized EESDs through DIW process.
- Although 3D DIW printing process offers an opportunity to develop high-performance microelectrodes from an electrochemical point of view, these can lack mechanical stability due to the generation of unavoidable porosity during the printing process. In addition, existence of an interface between the adjacent printed layers can cause large residual stresses in the printed microlattice architectures, which can also deteriorate their mechanical integrity rapidly. To avoid such circumstances, 2D-driven advanced composite inks in the existence of appropriate reinforcing additives or by applying post-treatment processes, such as additional thermal treatment, can be a suitable strategy to attain mechanically stable printed architectures.
- Importance of porous and well-interconnected hierarchical electrode materials cannot be denied as these facilitate shorter charge carrier pathways for the ultrafast movement of electrons/ions during electrochemical measurements and can effectively upgrade the electrochemical contribution of electrode materials. However, it is not an easy task to build highly porous hierarchical structures at the nano- or microscale. Therefore, more efforts are required to be devoted to manufacturing novel HR 3D-printed architectures with a lot of liberty to attain any required design and dimensions (nano/microscale). In this regard, combination of 2D-driven composite materials and 3D DIW printing process can be a vital breakthrough to generate hierarchically structured porous MEESDs with required ideal results.
- In recent times, 3D all-printed MEESDs have been manufactured by layer-by-layer deposition of the electroactive material, the current collector, and electrolyte inks via multi-nozzle DIW printing process. In realization of the development of safe 3D all-printed MEESD packages, a few challenges such as the leakage of moisture/air need to be resolved. Application of integrated, hybrid printing strategy can be vital in this regard.
- CE of the 3D-printed MEESDs is on the lower side in comparison to conventional bulk devices; owing to this drawback, the performance of the device can deteriorate at a faster rate, resulting in the failure of the microelectronics systems. In order to overcome this critical issue, it is required to mitigate the irreversible reactions by applying appropriate ink materials, controlling the porosity in the electrode architectures, modifying the surface chemistry of the electroactive materials, and regulating the electrolyte solutions.

- In the existence of 2D materials building blocks, advanced hierarchical microstructures need to be synthesized in order to empower the overall electrochemical output (such as ED, PD, and cycling stability) of printed hybrid supercapacitors. Moreover, void space is available in terms of the development of efficient next-generation flexible batteries with the aid of versatile manufacturing processes such as DIW printing techniques and highly versatile 2D-driven composite materials.

- Numbers of DIW-manufactured 2D-driven materials have been reported for MEESDs (e.g., MBs and MSCs); however, in-depth intrinsic electrochemical energy storage mechanisms (EES-Ms) have not yet been revealed comprehensively. It is widely established that the electrochemical contribution of printed electrode materials is highly related to their geometries. DIW printing process offers a good platform to digitally control the geometries of the electrode materials, wherein the energy storage mechanisms can be willingly investigated during the charge and discharge cycles. In this context, it is expected to devote more efforts to further boost the understanding of energy storage mechanisms.

- Integration of high-performance 3D-printed MEESDs with energy monitoring systems and energy harvesting systems is a potential research direction to consider in the future.

Thus, we emphasize that 3D printing process such as DIW with better resolution, application of a wide range of 2D materials, scalability, versatile production opportunities, and low cost will disclose new avenues in material designing and freedom to construct architectures for advanced MEESDs exhibiting excellent overall electrochemical performance, reliable mechanical strength, and customizable electrode configurations for other broad applications (such as miniaturized biomedical devices, microrobots, and flexible micro-electronics).

DECLARATIONS

Authors' contributions

Conceptualization, methodology, writing-original draft, revision, review & editing: Saeed G

Writing-original draft, investigation, visualization, data curation: Kang T, Byun JS

Visualization, literature survey, data curation: Min D, Kim JS

Visualization, investigation, data curation: Sadavar SV

Supervision, investigation, writing-review & editing: Park HS

Availability of data and materials

The data is available upon request.

Financial support and sponsorship

This work was financially supported by the National Research Foundation of Korea (NRF) grant funded by the Korean government (MSIT) (No. NRF-2020R1A3B2079803).

Conflict of interests

All authors declared that there are no conflicts of interest.

Ethical approval and consent to participate

Not applicable.

Consent for publication

Not applicable.

Copyright

© The Author(s) 2024.

REFERENCES

1. Zhu M, Schmidt OG. Tiny robots and sensors need tiny batteries-here's how to do it. *Nature* 2021;589:195-7. DOI PubMed
2. Yu L, Li W, Wei C, Yang Q, Shao Y, Sun J. 3D printing of NiCoP/Ti₃C₂MXene architectures for energy storage devices with high areal and volumetric energy density. *Nanomicro Lett* 2020;12:143. DOI PubMed PMC
3. Jin J, Geng X, Chen Q, Ren TL. A better Zn-Ion storage device: recent progress for Zn-Ion hybrid supercapacitors. *Nanomicro Lett* 2022;14:64. DOI PubMed PMC
4. Hur JI, Smith LC, Dunn B. High areal energy density 3D lithium-ion microbatteries. *Joule* 2018;2:1187-201. DOI
5. Zhang P, Wang F, Yu M, Zhuang X, Feng X. Two-dimensional materials for miniaturized energy storage devices: from individual devices to smart integrated systems. *Chem Soc Rev* 2018;47:7426-51. DOI
6. Pan X, Hong X, Xu L, Li Y, Yan M, Mai L. On-chip micro/nano devices for energy conversion and storage. *Nano Today* 2019;28:100764. DOI
7. Liu H, Zhang G, Zheng X, Chen F, Duan H. Emerging miniaturized energy storage devices for microsystem applications: from design to integration. *Int J Extrem Manuf* 2020;2:042001. DOI
8. Jia R, Shen G, Qu F, Chen D. Flexible on-chip micro-supercapacitors: efficient power units for wearable electronics. *Energy Stor Mater* 2020;27:169-86. DOI
9. Sumboja A, Liu J, Zheng WG, Zong Y, Zhang H, Liu Z. Electrochemical energy storage devices for wearable technology: a rationale for materials selection and cell design. *Chem Soc Rev* 2018;47:5919-45. DOI PubMed
10. Chang Kim M, Saeed G, Alam A, et al. Ultrafine nanoparticles of tin-cobalt-sulfide decorated over 2D MXene sheets as a cathode material for high-performance asymmetric supercapacitor. *J Ind Eng Chem* 2023;124:294-303. DOI
11. Zhang L, Yu L, Li OL, et al. FeF₃·0.33H₂O@C nanocomposites derived from pomegranate structure as high-performance cathodes for sodium- and lithium-ion batteries. *Jops* 2022;547:232014. DOI
12. Yu L, Kim KS, Saeed G, Kang J, Kim KH. Hybrid ZnSe-SnSe₂ nanoparticles embedded in N-doped carbon nanocube heterostructures with enhanced and ultra-stable lithium-storage performance. *ChemElectroChem* 2021;8:4732-44. DOI
13. Brown E, Yan P, Tekik H, et al. 3D printing of hybrid MoS₂-graphene aerogels as highly porous electrode materials for sodium ion battery anodes. *Mater Design* 2019;170:107689. DOI
14. Delmas C. Sodium and sodium-ion batteries: 50 years of research. *Adv Energy Mater* 2018;8:1703137. DOI
15. Zhu Z, Kan R, Hu S, et al. Recent advances in high-performance microbatteries: construction, application, and perspective. *Small* 2020;16:e2003251. DOI PubMed
16. Zhang L, Liu D, Wu Z, Lei W. Micro-supercapacitors powered integrated system for flexible electronics. *Energy Stor Mater* 2020;32:402-17. DOI
17. Chhowalla M, Shin HS, Eda G, Li LJ, Loh KP, Zhang H. The chemistry of two-dimensional layered transition metal dichalcogenide nanosheets. *Nat Chem* 2013;5:263-75. DOI PubMed
18. Peng X, Peng L, Wu C, Xie Y. Two dimensional nanomaterials for flexible supercapacitors. *Chem Soc Rev* 2014;43:3303-23. DOI PubMed
19. Shao M, Zhang R, Li Z, Wei M, Evans DG, Duan X. Layered double hydroxides toward electrochemical energy storage and conversion: design, synthesis and applications. *Chem Commun* 2015;51:15880-93. DOI
20. Zhang H. Ultrathin two-dimensional nanomaterials. *ACS Nano* 2015;9:9451-69. DOI PubMed
21. Novoselov KS, Geim AK, Morozov SV, et al. Electric field effect in atomically thin carbon films. *Science* 2004;306:666-9. DOI
22. Zhang Y, Tan YW, Stormer HL, Kim P. Experimental observation of the quantum Hall effect and Berry's phase in graphene. *Nature* 2005;438:201-4. DOI PubMed
23. Akinwande D, Petrone N, Hone J. Two-dimensional flexible nanoelectronics. *Nat Commun* 2014;5:5678. DOI PubMed
24. Ambrosi A, Pumera M. 3D-printing technologies for electrochemical applications. *Chem Soc Rev* 2016;45:2740-55. DOI PubMed
25. Qiu L, He Z, Li D. Multifunctional cellular materials Based on 2D nanomaterials: prospects and challenges. *Adv Mater* 2018;30:1704850. DOI
26. Garg R, Agarwal A, Agarwal M. A review on MXene for energy storage application: effect of interlayer distance. *Mater Res Express* 2020;7:022001. DOI
27. Li K, Liang M, Wang H, et al. 3D MXene architectures for efficient energy storage and conversion. *Adv Funct Mater* 2020;30:2000842. DOI
28. Talaie E, Bonnick P, Sun X, Pang Q, Liang X, Nazar LF. Methods and protocols for electrochemical energy storage materials research. *Chem Mater* 2017;29:90-105. DOI
29. Zhou X, Cao A, Wan L, Guo Y. Spin-coated silicon nanoparticle/graphene electrode as a binder-free anode for high-performance lithium-ion batteries. *Nano Res* 2012;5:845-53. DOI
30. Zheng S, Shi X, Das P, Wu ZS, Bao X. The road towards planar microbatteries and micro-supercapacitors: from 2D to 3D device geometries. *Adv Mater* 2019;31:e1900583. DOI PubMed
31. Wang Z, Chen Y, Zhou Y, Ouyang J, Xu S, Wei L. Miniaturized lithium-ion batteries for on-chip energy storage. *Nanoscale Adv*

- 2022;4:4237-57. DOI PubMed PMC
32. Zhang W, Liu H, Zhang X, Li X, Zhang G, Cao P. 3D printed micro-electrochemical energy storage devices: from design to integration. *Adv Funct Mater* 2021;31:2104909. DOI
 33. Jabbar Khan A, Mateen A, Khan S, et al. 3D printed micro-electrochemical energy storage devices. *Batteries Supercaps* 2023;6:e202300190. DOI
 34. Bounor B, Asbani B, Douard C, Favier F, Brousse T, Lethien C. On chip MnO₂-based 3D micro-supercapacitors with ultra-high areal energy density. *Energy Stor Mater* 2021;38:520-7. DOI
 35. Xu Y, Sheng K, Li C, Shi G. Self-assembled graphene hydrogel via a one-step hydrothermal process. *ACS Nano* 2010;4:4324-30. DOI PubMed
 36. Xiong C, Li B, Lin X, et al. The recent progress on three-dimensional porous graphene-based hybrid structure for supercapacitor. *Compos Part B-Eng* 2019;165:10-46. DOI
 37. Ashby DS, Deblock RH, Lai C, Choi CS, Dunn BS. Patternable, solution-processed ionogels for thin-film lithium-ion electrolytes. *Joule* 2017;1:344-58. DOI
 38. Alam A, Saeed G, Kim KH, Lim S. Metal-organic framework-derived NiS@Cobalt-Molybdenum layered double hydroxides shell@core as cathode and CoFe₂O₄-nanoparticles@MXene shell@core as anode materials for ultra-high energy-density flexible asymmetric supercapacitor. *J Energy Stor* 2022;55:105592. DOI
 39. Soram BS, Dai JY, Thangjam IS, Kim NH, Lee JH. One-step electrodeposited MoS₂@Ni-mesh electrode for flexible and transparent asymmetric solid-state supercapacitors. *J Mater Chem A* 2020;8:24040-52. DOI
 40. Wang L, Wang Q, Jia W, Chen S, Gao P, Li J. Li metal coated with amorphous Li₃PO₄ via magnetron sputtering for stable and long-cycle life lithium metal batteries. *J Power Sources* 2017;342:175-82. DOI
 41. Gandla D, Tan DQ. Progress report on atomic layer deposition toward hybrid nanocomposite electrodes for next generation supercapacitors. *Adv Mater Inter* 2019;6:1900678. DOI
 42. Saeed G, Kumar S, Kim NH, Lee JH. Fabrication of 3D graphene-CNTs/ α -MoO₃ hybrid film as an advance electrode material for asymmetric supercapacitor with excellent energy density and cycling life. *Chem Eng J* 2018;352:268-76. DOI
 43. Lobe S, Bauer A, Uhlenbruck S, Fattakhova-Rohlfing D. Physical vapor deposition in solid-state battery development: from materials to devices. *Adv Sci* 2021;8:e2002044. DOI PubMed PMC
 44. Zeng L, Li P, Yao Y, Niu B, Niu S, Xu B. Recent progresses of 3D printing technologies for structural energy storage devices. *Mater Today Nano* 2020;12:100094. DOI
 45. Zhang F, Wei M, Viswanathan VV, et al. 3D printing technologies for electrochemical energy storage. *Nano Energy* 2017;40:418-31. DOI
 46. Egorov V, Gulzar U, Zhang Y, Breen S, O'Dwyer C. Evolution of 3D printing methods and materials for electrochemical energy storage. *Adv Mater* 2020;32:e2000556. DOI PubMed
 47. Cheng M, Deivanayagam R, Shahbazian-yassar R. 3D printing of electrochemical energy storage devices: a review of printing techniques and electrode/electrolyte architectures. *Batteries Supercaps* 2020;3:130-46. DOI
 48. Gao T, Zhou Z, Yu J, et al. 3D printing of tunable energy storage devices with both high areal and volumetric energy densities. *Adv Energy Mater* 2019;9:1802578. DOI
 49. Guo B, Liang G, Yu S, Wang Y, Zhi C, Bai J. 3D printing of reduced graphene oxide aerogels for energy storage devices: a paradigm from materials and technologies to applications. *Energy Stor Mater* 2021;39:146-65. DOI
 50. Guo H, Lv R, Bai S. Recent advances on 3D printing graphene-based composites. *Nano Mater Sci* 2019;1:101-15. DOI
 51. Wang J, Liu Y, Fan Z, Wang W, Wang B, Guo Z. Ink-based 3D printing technologies for graphene-based materials: a review. *Adv Compos Hybrid Mater* 2019;2:1-33. DOI
 52. Pang Y, Cao Y, Chu Y, et al. Additive manufacturing of batteries. *Adv Funct Mater* 2020;30:1906244. DOI
 53. Tagliaferri S, Panagiotopoulos A, Mattevi C. Direct ink writing of energy materials. *Mater Adv* 2021;2:540-63. DOI
 54. Tian X, Jin J, Yuan S, Chua CK, Tor SB, Zhou K. Emerging 3D-printed electrochemical energy storage devices: a critical review. *Adv Energy Mater* 2017;7:1700127. DOI
 55. Xu X, Tan YH, Ding J, Guan C. 3D printing of next-generation electrochemical energy storage devices: from multiscale to multimaterial. *Energy Environ Mater* 2022;5:427-38. DOI
 56. Zhu C, Liu T, Qian F, et al. 3D printed functional nanomaterials for electrochemical energy storage. *Nano Today* 2017;15:107-20. DOI
 57. Yao B, Chandrasekaran S, Zhang J, et al. Efficient 3D printed pseudocapacitive electrodes with ultrahigh MnO₂ loading. *Joule* 2019;3:459-70. DOI
 58. Zeng L, Ling S, Du D, He H, Li X, Zhang C. Direct ink writing 3D printing for high-performance electrochemical energy storage devices: a minireview. *Adv Sci* 2023;10:2303716. DOI
 59. Wei M, Zhang F, Wang W, Alexandridis P, Zhou C, Wu G. 3D direct writing fabrication of electrodes for electrochemical storage devices. *Jops* 2017;354:134-47. DOI
 60. Lyu Z, Lim GJ, Koh JJ, et al. Design and manufacture of 3D-printed batteries. *Joule* 2021;5:89-114. DOI
 61. Kim H, Johnson J, Chavez LA, Garcia Rosales CA, Tseng TB, Lin Y. Enhanced dielectric properties of three phase dielectric MWCNTs/BaTiO₃/PVDF nanocomposites for energy storage using fused deposition modeling 3D printing. *Ceram Int* 2018;44:9037-44. DOI

62. Maurel A, Russo R, Grugeon S, Panier S, Dupont L. Environmentally friendly lithium-terephthalate/poly(lactic acid) composite filament formulation for lithium-ion battery 3D-printing via fused deposition modeling. *ECS J Solid State Sci Technol* 2021;10:037004. DOI
63. Szymela K, Bienia M, Rossignol F, et al. Fabrication of modern lithium ion batteries by 3D inkjet printing: opportunities and challenges. *Heliyon* 2022;8:e12623. DOI PubMed PMC
64. Pei M, Shi H, Yao F, et al. 3D printing of advanced lithium batteries: a designing strategy of electrode/electrolyte architectures. *J Mater Chem A* 2021;9:25237-57. DOI
65. Gulzar U, Glynn C, O'dwyer C. Additive manufacturing for energy storage: methods, designs and material selection for customizable 3d printed batteries and supercapacitors. *Curr Opin Electrochem* 2020;20:46-53. DOI
66. Gokhare VG, Raut DN, Shinde DK. A review paper on 3D-printing aspects and various processes used in the 3D-printing. Available from: <https://www.ijert.org/a-review-paper-on-3d-printing-aspects-and-various-processes-used-in-the-3d-printing> [Last accessed on 7 Mar 2024].
67. Ge Q, Li Z, Wang Z, et al. Projection micro stereolithography based 3D printing and its applications. *Int J Extrem Manuf* 2020;2:022004. DOI
68. Katsuyama Y, Haba N, Kobayashi H, et al. Macro- and nano-porous 3D-hierarchical carbon lattices for extraordinarily high capacitance supercapacitors. *Adv Funct Mater* 2022;32:2201544. DOI
69. Li L, Deng Z, Chen M, Yu ZZ, Russell TP, Zhang HB. 3D Printing of ultralow-concentration 2D nanomaterial inks for multifunctional architectures. *Nano Lett* 2023;23:155-62. DOI
70. Sahoo R, Pal A, Pal T. 2D materials for renewable energy storage devices: outlook and challenges. *Chem Commun* 2016;52:13528-42. DOI
71. Dong Y, Wu ZS, Ren W, Cheng HM, Bao X. Graphene: a promising 2D material for electrochemical energy storage. *Sci Bull* 2017;62:724-40. DOI PubMed
72. Wang L, Chen S, Shu T, Hu X. Functional Inks for printable energy storage applications based on 2D materials. *ChemSusChem* 2020;13:1330-53. DOI
73. Naficy S, Jalili R, Aboutalebi SH, et al. Graphene oxide dispersions: tuning rheology to enable fabrication. *Mater Horiz* 2014;1:326-31. DOI
74. Jiang Y, Guo F, Liu Y, Xu Z, Gao C. Three-dimensional printing of graphene-based materials for energy storage and conversion. *SusMat* 2021;1:304-23. DOI
75. Tian X. Direct ink writing of 2D material-based supercapacitors. *2D Mater* 2022;9:012001. DOI
76. Xie Y, Zhang H, Huang H, et al. High-voltage asymmetric MXene-based on-chip micro-supercapacitors. *Nano Energy* 2020;74:104928. DOI
77. Zhu Y, Wang S, Ma J, Das P, Zheng S, Wu Z. Recent status and future perspectives of 2D MXene for micro-supercapacitors and micro-batteries. *Energy Stor Mater* 2022;51:500-26. DOI
78. Zhang CJ, McKeon L, Kremer MP, et al. Additive-free MXene inks and direct printing of micro-supercapacitors. *Nat Commun* 2019;10:1795. DOI PubMed PMC
79. Yang W, Yang J, Byun JJ, et al. 3D printing of freestanding MXene architectures for current-collector-free supercapacitors. *Adv Mater* 2019;31:e1902725. DOI PubMed
80. Akuzum B, Maleski K, Anasori B, et al. Rheological characteristics of 2D titanium carbide (MXene) dispersions: a guide for processing MXenes. *ACS Nano* 2018;12:2685-94. DOI
81. Bao C, Zhang H, Wilkie CA, et al. On the dispersion systems of graphene-like two-dimensional materials: From fundamental laws to engineering guidelines. *Carbon* 2016;107:774-82. DOI
82. García-Tuñón E, Feilden E, Zheng H, D'Elia E, Leong A, Saiz E. Graphene oxide: an all-in-one processing additive for 3D printing. *ACS Appl Mater Interfaces* 2017;9:32977-89. DOI PubMed
83. Panagiotopoulos A, Nagaraju G, Tagliaferri S, et al. 3D printed inks of two-dimensional semimetallic MoS₂/TiS₂ nanosheets for conductive-additive-free symmetric supercapacitors. *J Mater Chem A* 2023;11:16190-200. DOI
84. Zhou G, Li M, Liu C, Wu Q, Mei C. 3D printed Ti₃C₂ TxMXene/cellulose nanofiber architectures for solid-state supercapacitors: ink rheology, 3D printability, and electrochemical performance. *Adv Funct Mater* 2022;32:2109593. DOI
85. Tang X, Zhou H, Cai Z, et al. Generalized 3D printing of graphene-based mixed-dimensional hybrid aerogels. *ACS Nano* 2018;12:3502-11. DOI
86. Yao B, Chandrasekaran S, Zhang H, et al. 3D-printed structure boosts the kinetics and intrinsic capacitance of pseudocapacitive graphene aerogels. *Adv Mater* 2020;32:e1906652. DOI PubMed
87. Zheng Y, Zhao W, Jia D, Cui L, Liu J. Thermally-treated and acid-etched carbon fiber cloth based on pre-oxidized polyacrylonitrile as self-standing and high area-capacitance electrodes for flexible supercapacitors. *Chem Eng J* 2019;364:70-8. DOI
88. Zhu C, Liu T, Qian F, et al. Supercapacitors based on three-dimensional hierarchical graphene aerogels with periodic macropores. *Nano Lett* 2016;16:3448-56. DOI
89. Chandrasekaran S, Yao B, Liu T, et al. Direct ink writing of organic and carbon aerogels. *Mater Horiz* 2018;5:1166-75. DOI
90. Wang G, Wang H, Lu X, et al. Solid-state supercapacitor based on activated carbon cloths exhibits excellent rate capability. *Adv Mater* 2014;26:2676-82, 2615. DOI PubMed
91. Wang Y, Zhang Y, Wang G, et al. Direct graphene-carbon nanotube composite ink writing all-solid-state flexible

- microsupercapacitors with high areal energy density. *Adv Funct Mater* 2020;30:1907284. DOI
92. Nakhanivej P, Dou Q, Xiong P, Park HS. Two-dimensional pseudocapacitive nanomaterials for high-energy- and high-power-oriented applications of supercapacitors. *ACC Mater Res* 2021;2:86-96. DOI
93. Kyeremateng NA, Brousse T, Pech D. Microsupercapacitors as miniaturized energy-storage components for on-chip electronics. *Nat Nanotechnol* 2017;12:7-15. DOI PubMed
94. Kamboj N, Purkait T, Das M, Sarkar S, Hazra KS, Dey RS. Ultralong cycle life and outstanding capacitive performance of a 10.8 V metal free micro-supercapacitor with highly conducting and robust laser-irradiated graphene for an integrated storage device. *Energy Environ Sci* 2019;12:2507-17. DOI
95. Jiang Y, Xu Z, Huang T, et al. Direct 3D printing of ultralight graphene oxide aerogel microlattices. *Adv Funct Mater* 2018;28:1707024. DOI
96. Bhojane P. Recent advances and fundamentals of pseudocapacitors: materials, mechanism, and its understanding. *J Energy Stor* 2022;45:103654. DOI
97. Kim HS, Cook JB, Lin H, et al. Oxygen vacancies enhance pseudocapacitive charge storage properties of $\text{MoO}_{3,x}$. *Nat Mater* 2017;16:454-60. DOI PubMed
98. Wang Y, Wang M, Wang P, et al. Urea-treated wet-spun PEDOT: PSS fibers for achieving high-performance wearable supercapacitors. *Compos Commun* 2021;27:100885. DOI
99. Augustyn V, Simon P, Dunn B. Pseudocapacitive oxide materials for high-rate electrochemical energy storage. *Energy Environ Sci* 2014;7:1597. DOI
100. Lai F, Miao YE, Huang Y, Zhang Y, Liu T. Nitrogen-doped carbon nanofiber/molybdenum disulfide nanocomposites derived from bacterial cellulose for high-efficiency electrocatalytic hydrogen evolution reaction. *ACS Appl Mater Interfaces* 2016;8:3558-66. DOI PubMed
101. Saeed G, Bandyopadhyay P, Kumar S, Kim NH, Lee JH. $\text{ZnS-Ni}_3\text{S}_6$ nanosheet arrays wrapped with nanopetals of $\text{Ni}(\text{OH})_2$ as a novel core-shell electrode material for asymmetric supercapacitors with high energy density and cycling stability performance. *ACS Appl Mater Interfaces* 2020;12:47377-88. DOI PubMed
102. Alam A, Saeed G, Lim S. One-step synthesis of 2D-2D $\text{Co}(\text{OH})_2$ - MoSe_2 hybrid nanosheets as an efficient electrode material for high-performance asymmetric supercapacitor. *J Electroanal Chem* 2020;879:114775. DOI
103. Kumar KS, Choudhary N, Jung Y, Thomas J. Recent advances in two-dimensional nanomaterials for supercapacitor electrode applications. *ACS Energy Lett* 2018;3:482-95. DOI
104. Zong W, Ouyang Y, Miao YE, Liu T, Lai F. Recent advances and perspectives of 3D printed micro-supercapacitors: from design to smart integrated devices. *Chem Commun* 2022;58:2075-95. DOI PubMed
105. Huang X, Huang J, Yang D, Wu P. A multi-scale structural engineering strategy for high-performance MXene hydrogel supercapacitor electrode. *Adv Sci* 2021;8:e2101664. DOI PubMed PMC
106. Yao B, Peng H, Zhang H, et al. Printing porous carbon aerogels for low temperature supercapacitors. *Nano Lett* 2021;21:3731-7. DOI
107. Yu L, Fan Z, Shao Y, Tian Z, Sun J, Liu Z. Versatile N-doped MXene ink for printed electrochemical energy storage application. *Adv Energy Mater* 2019;9:1901839. DOI
108. Orangi J, Hamade F, Davis VA, Beidaghi M. 3D printing of additive-free 2D $\text{Ti}_3\text{C}_2\text{T}_x$ (MXene) ink for fabrication of micro-supercapacitors with ultra-high energy densities. *ACS Nano* 2020;14:640-50. DOI PubMed
109. Sadavar S, Wang KJ, Kang T, et al. Anion storage for hybrid supercapacitor. *Mater Today Energy* 2023;37:101388. DOI
110. Zhao J, Zhang Y, Lu H, et al. Additive manufacturing of two-dimensional conductive metal-organic framework with multidimensional hybrid architectures for high-performance energy storage. *Nano Lett* 2022;22:1198-206. DOI PubMed
111. Yang Z, Yang X, Yang T, et al. 3D printing of carbon tile-modulated well-interconnected hierarchically porous pseudocapacitive electrode. *Energy Stor Mater* 2023;54:51-9. DOI
112. Zhao J, Zhang Y, Zhao X, et al. Direct ink writing of adjustable electrochemical energy storage device with high gravimetric energy densities. *Adv Funct Mater* 2019;29:1900809. DOI
113. Zhang C, Kremer MP, Seral-ascaso A, et al. Stamping of flexible, coplanar micro-supercapacitors using MXene inks. *Adv Funct Mater* 2018;28:1705506. DOI
114. Zhao Y, Liu F, Zhu K, Maganti S, Zhao Z, Bai P. Three-dimensional printing of the copper sulfate hybrid composites for supercapacitor electrodes with ultra-high areal and volumetric capacitances. *Adv Compos Hybrid Mater* 2022;5:1537-47. DOI
115. Pender JP, Jha G, Youn DH, et al. Electrode degradation in lithium-ion batteries. *ACS Nano* 2020;14:1243-95. DOI
116. Chen C, Jiang M, Zhou T, et al. Interface aspects in all-solid-state Li-based batteries reviewed. *Adv Energy Mater* 2021;11:2003939. DOI
117. Imanishi N, Yamamoto O. Rechargeable lithium-air batteries: characteristics and prospects. *Mater Today* 2014;17:24-30. DOI
118. Yang R, Zhou J, Yang C, Qiu L, Cheng H. Recent progress in 3D printing of 2D material-based macrostructures. *Adv Mater Tech* 2020;5:1901066. DOI
119. Ye J, Baumgaertel AC, Wang YM, Biener J, Biener MM. Structural optimization of 3D porous electrodes for high-rate performance lithium ion batteries. *ACS Nano* 2015;9:2194-202. DOI PubMed
120. Zhang H, Yu X, Braun PV. Three-dimensional bicontinuous ultrafast-charge and -discharge bulk battery electrodes. *Nat Nanotechnol* 2011;6:277-81. DOI

121. Hassan K, Nine MJ, Tung TT, et al. Functional inks and extrusion-based 3D printing of 2D materials: a review of current research and applications. *Nanoscale* 2020;12:19007-42. [DOI](#)
122. Sun C, Liu S, Shi X, Lai C, Liang J, Chen Y. 3D printing nanocomposite gel-based thick electrode enabling both high areal capacity and rate performance for lithium-ion battery. *Chem Eng J* 2020;381:122641. [DOI](#)
123. Rosenman A, Markevich E, Salitra G, Aurbach D, Garsuch A, Chesneau FF. Review on Li-sulfur battery systems: an integral perspective. *Adv Energy Mater* 2015;5:1500212. [DOI](#)
124. Shen K, Mei H, Li B, Ding J, Yang S. 3D printing sulfur copolymer-graphene architectures for Li-S batteries. *Adv Energy Mater* 2018;8:1701527. [DOI](#)
125. Chen C, Jiang J, He W, Lei W, Hao Q, Zhang X. 3D printed high-loading lithium-sulfur battery toward wearable energy storage. *Adv Funct Mater* 2020;30:1909469. [DOI](#)
126. Liu B, Zhang J, Xu W. Advancing lithium metal batteries. *Joule* 2018;2:833-45. [DOI](#)
127. Ma J, Zheng S, Zhou F, et al. All 3D printing lithium metal batteries with hierarchically and conductively porous skeleton for ultrahigh areal energy density. *Energy Stor Mater* 2023;54:304-12. [DOI](#)
128. Shen K, Cao Z, Shi Y, Zhang Y, Li B, Yang S. 3D printing lithium salt towards dendrite-free lithium anodes. *Energy Stor Mater* 2021;35:108-13. [DOI](#)
129. Lyu Z, Lim GJ, Guo R, et al. 3D-printed electrodes for lithium metal batteries with high areal capacity and high-rate capability. *Energy Stor Mater* 2020;24:336-42. [DOI](#)
130. Gao X, Yang X, Wang S, et al. A 3D-printed ultra-high Se loading cathode for high energy density quasi-solid-state Li-Se batteries. *J Mater Chem A* 2020;8:278-86. [DOI](#)
131. Cai J, Jin J, Fan Z, et al. 3D Printing of a V_8C_7 - VO_2 Bifunctional scaffold as an effective polysulfide immobilizer and lithium stabilizer for Li-S batteries. *Adv Mater* 2020;32:e2005967. [DOI](#)
132. Mubarak S, Dhamodharan D, Byun H. Recent advances in 3D printed electrode materials for electrochemical energy storage devices. *J Energy Chem* 2023;81:272-312. [DOI](#)
133. Bu F, Li C, Wang Q, Liu X. Ultraviolet-assisted printing of flexible all-solid-state zinc batteries with enhanced interfacial bond. *Chem Eng J* 2022;449:137710. [DOI](#)
134. Hwang JY, Myung ST, Sun YK. Sodium-ion batteries: present and future. *Chem Soc Rev* 2017;46:3529-614. [DOI](#)
135. Zhang T, Tang Y, Guo S, et al. Fundamentals and perspectives in developing zinc-ion battery electrolytes: a comprehensive review. *Energy Environ Sci* 2020;13:4625-65. [DOI](#)
136. Jia X, Liu C, Neale ZG, Yang J, Cao G. Active materials for aqueous zinc ion batteries: synthesis, crystal structure, morphology, and electrochemistry. *Chem Rev* 2020;120:7795-866. [DOI](#)
137. Lourenssen K, Williams J, Ahmadpour F, Clemmer R, Tasnim S. Vanadium redox flow batteries: a comprehensive review. *J Energy Stor* 2019;25:100844. [DOI](#)
138. Zhu Y, Peng L, Fang Z, Yan C, Zhang X, Yu G. Structural engineering of 2D nanomaterials for energy storage and catalysis. *Adv Mater* 2018;30:e1706347. [DOI](#)
139. Pomerantseva E, Bonaccorso F, Feng X, Cui Y, Gogotsi Y. Energy storage: the future enabled by nanomaterials. *Science* 2019;366:eaan8285. [DOI](#) [PubMed](#)
140. Wang Z, Huang Z, Wang H, et al. 3D-printed sodiophilic V_2CT_x/rGO -CNT MXene microgrid aerogel for stable Na metal anode with high areal capacity. *ACS Nano* 2022;16:9105-16. [DOI](#)
141. Li Q, Dong Q, Wang J, et al. Direct ink writing (DIW) of graphene aerogel composite electrode for vanadium redox flow battery. *Jops* 2022;542:231810. [DOI](#)
142. Ma H, Tian X, Wang T, et al. Tailoring pore structures of 3D printed cellular high-loading cathodes for advanced rechargeable Zinc-Ion batteries. *Small* 2021;17:e2100746. [DOI](#) [PubMed](#)
143. Yang H, Wang H, Li W, et al. A simple and effective host for sodium metal anode: a 3D-printed high pyrrolic-N doped graphene microlattice aerogel. *J Mater Chem A* 2022;10:16842-52. [DOI](#)
144. Ma J, Zheng S, Chi L, et al. 3D printing flexible sodium-ion microbatteries with ultrahigh areal capacity and robust rate capability. *Adv Mater* 2022;34:e2205569. [DOI](#)
145. Yan J, Zhi G, Kong D, et al. 3D printed rGO/CNT microlattice aerogel for a dendrite-free sodium metal anode. *J Mater Chem A* 2020;8:19843-54. [DOI](#)